

Wavelet Theory and some of its Applications

Elin Johansson

Luleå University of Technology
Department of Mathematics

Wavelet Theory and some of its Applications

by

Elin Johansson

Department of Mathematics
Luleå University of Technology
S-971 87 Luleå, Sweden

February 2005

Supervisor

Professor Lars-Erik Persson
Luleå University of Technology, Sweden

Published 2005

Printed in Sweden by University Printing Office, Luleå

Abstract

This thesis deals with applied mathematics with wavelets as a joint subject. There is an introduction and two extensive papers, of which one is already published in an international journal. The introduction presents wavelet theory including both the discrete and continuous wavelet transforms, the corresponding Fourier transforms, wavelet packets and the uncertainty principle. Moreover, it is a guide to applications. We consider applications that are strongly connected to the thesis and other too, but more briefly. Also, the connection to both of the papers is included in the introduction.

Paper 1 considers irregular sampling in shift-invariant spaces, such as for instance the spaces that are connected to a multiresolution analysis within wavelet theory. We set out the necessary theoretical aspects to enable reconstruction of an irregularly sampled function. Unlike most previous work in this area the method that is proposed in Paper 1 opens up for comparatively easy calculations of examples. Accordingly, we give a thorough exposition of one example of a sampling function.

Paper 2 contains derivation and comparison of several different vibration analysis techniques for automatic detection of local defects in bearings. An extensive number of mathematical methods are suggested and evaluated through tests with both laboratory and industrial environment signals. Two out of the four best methods found are wavelet based, with an error rate of about 10%. Finally, there are many potentially performance improving additions included.

Acknowledgements

First of all I would like to thank my main supervisor Professor Lars-Erik Persson for his commitment, inspiring enthusiasm, and faith in me during my years as a Ph.D. student.

Secondly, my deepest gratitude to my assisting supervisor Ph.D. Stefan Ericsson who has spent endless hours guiding me, questioning my work, discussing and explaining mathematics in general and the connection to the problem at hand in particular.

Next, I want to thank my co-authors Ph.D. Stefan Ericsson, Ph.D Niklas Grip, Professor Lars-Erik Persson, M.Sc. Ronny Sjöberg at SKF Condition Monitoring Center Luleå, and Professor Jan-Olof Strömberg at KTH for fruitful cooperation and a both challenging and instructive period of work.

Also, my colleagues at the Department of Mathematics at Luleå University of Technology deserves recognition for good companionship. A sincere thanks to my friend and colleague Maria Johansson for priceless moments of support and for sharing both good and bad moments in life. Also, the computer support, especially Andreas Nilsson, deserves a thanks for all his help with the technical "details".

Finally, I would like to thank Tomas for his constant love and support. I would not have done this without you.

Preface

This thesis consists of an introductory part "Introduction - Some Wavelet Theory and a Guide to Applications" and the following papers:

- Paper 1

E. Johansson, "Sampling in Shift-Invariant Spaces", research report, Department of Mathematics, Luleå University of Technology, 2005 (21 pages).

- Paper 2

S. Ericsson, N. Grip, E. Johansson, L.E. Persson, R. Sjöberg, J.O. Strömberg, "Towards automatic detection of local bearing defects in rotating machines". Mechanical Systems and Signal Processing, Vol. 19 (2005), 509-535.

Remark: Paper 2 is the result of a cooperation between KTH, LTU and SKF Condition Monitoring Center Luleå, formerly Nåiden Teknik AB.

Contents

Abstract	iii
Acknowledgements	v
Preface	vii
Introduction - Some Wavelet Theory and a Guide to Applications	1
1 Frequency Analysis	2
2 Time-frequency Analysis	3
2.1 Short Time Fourier Transform	3
2.2 Wavelet Analysis	4
2.3 Uncertainty Principles	5
2.4 Discrete Wavelet Transform	7
2.5 Wavelet Packets	10
2.6 Final Remarks on Applications	11
Papers	15
1 Sampling in Shift-Invariant Spaces	17
2 Towards automatic detection of local bearing defects in rotating machines	41

Introduction - Some Wavelet Theory and a Guide to Applications

This introduction is an overview of wavelets and a theoretical support and complement to the articles in the thesis.

The mathematical tool *wavelet transform*, and the theoretical framework for wavelets in general, has been widely developed since its breakthrough in the mid eighties and used in a variety of areas of sciences.

We will start by describing the frequency analysis tool Fourier transform in Section 1. Analyzing a signal with the Fourier transform leads to information about the frequency spectrum, i.e. which frequencies and how much of each frequency the signal contains. However, the standard form to analyze the Fourier transform is to study the behavior of $|\hat{f}(\omega)|$, which does not refer to at what time the phenomenon that cause the frequency peak(s) occur. Also, small transient outbursts give almost not noticeable contribution to the frequency spectra since it is the average of the frequencies that is measured.

Wavelet analysis, on the other hand, supplies information about both time and frequency, although both parameters cannot be exactly determined simultaneously due to the *Heisenberg uncertainty relation*. This is presented in Section 2.

Analytically, one can use the continuous version of various mathematical transforms, but computer aided analysis require sampled signals and consequently the discrete versions of the transforms. Therefore, both continuous and discrete transforms will be presented. Also, an introduction to the special case wavelet packets is given in Section 2.5.

At a number of points, there will be some historical notes and an orientation to applications.

1 Frequency Analysis

This section describes the most common frequency analysis method, the Fourier transform, in its different shapes. For stationary signals, it is an optimal method to analyze the frequency content. The Fourier transform is named after its inventor Joseph Fourier and is dated to the early 1800's.

Definition 1 (Continuous Fourier Transform) *The Continuous Fourier Transform (CFT) of a function f is defined by*

$$\hat{f}(\omega) = \int_{\mathbb{R}} f(x) e^{-i\omega x} dx,$$

and its inverse Fourier transform by

$$f(x) = \frac{1}{2\pi} \int_{\mathbb{R}} \hat{f}(\omega) e^{i\omega x} d\omega.$$

We conclude that $\hat{f}(\omega)$ gives the amplitude of each sinusoidal wave $e^{i\omega t}$ in the function $f(t)$.

In addition to its frequency analysis properties the Fourier transform has some useful mathematical relations, e.g. convolution in the time domain corresponds to multiplication in the frequency domain. Hence, the CFT may be used in mathematical derivations, such as for instance in Section 6, Paper 1.

For discrete signals $f[n]$, sampled from $f(x)$ in Definition 1, we need the *Discrete Fourier Transform* (DFT).

Definition 2 (Discrete Fourier Transform) *The discrete Fourier transform $\hat{f}[k]$ of a N -periodic signal $f[n]$ is defined by*

$$\hat{f}[k] = \frac{1}{N} \sum_{n=0}^{N-1} f[n] e^{-i2\pi kn/N},$$

and the inverse transform by

$$f[n] = \sum_{k=0}^{N-1} \hat{f}[k] e^{i2\pi kn/N}.$$

Note that the DFT is adapted to signals from real applications, which always have finite length. To avoid difficulties in the ends, the signal is repeated, thus made periodic. There is a famous method to calculate the DFT. This method is

called the *Fast Fourier Transform* (FFT) and it calculates the DFT with as little as $O(N \ln N)$ operations when the period N meets the requirement $N = 2^m$.

A concluding remark is that the Fourier transform is a method very well suited for stationary signals, but not as well for signals including transient phenomena. It is, however, an important part of signal processing and has been used in almost every application imaginable, including the bearing monitoring system that was aimed to be improved by wavelet techniques in Paper 2.

For a more thorough description of the Fourier transform, see for instance [1, 4, 13, 18].

2 Time-frequency Analysis

The decomposition of a function when a time perspective is preferred in addition to information about frequency content is called time-frequency analysis. A good example of a device that performs such analysis is the human ear, see [9], which gives information about what happens, and when, in the surroundings. Also in [10, 12] there are examples connected to music and hearing to give an intuitive understanding of time-frequency analysis.

2.1 Short Time Fourier Transform

One possible way to estimate the frequency contents of $f(x)$ at an arbitrary time $x = t$ is to cut off a piece of f and compute the Fourier transform of this piece only. This is called *Short Time Fourier Transform* (STFT), as in [10], or sometimes *Windowed Fourier Transform*, as in [13]. Both notations are easily argued for since it is a Fourier transform on a short piece of the function, i.e. during a short period of time and the restriction in time may be viewed as a translated window.

In Figure 1 the cutting is done, as described in [8, 10], by multiplication with a window function $\overline{g(x-t)}$, located at $x = t$. Here, overlining denotes the complex conjugate.

Definition 3 (Short Time Fourier Transform) *The Short Time Fourier Transform of a function f with respect to g is defined as*

$$V_g f(t, \xi) = \int_{\mathbb{R}} f(x) \overline{g_{t,\xi}(x)} dx, \quad \text{for } t, \xi \in \mathbb{R},$$

where $g_{t,\xi}(x) = e^{i\xi x} g(x-t)$ and $g \neq 0$ is a fix, real and symmetric, window function.

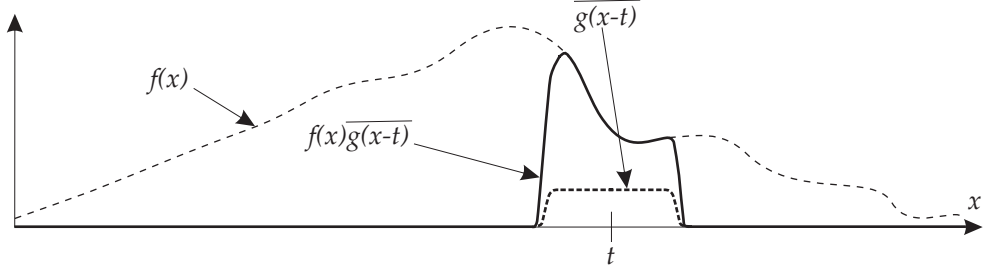


Figure 1: Time-frequency analysis with the STFT and continuous wavelet transform.

We will now look at a definition of the localization or time and frequency spread of the window function g .

Definition 4 (Time-frequency localization) *The function g has the time spread $\sigma_x(g)$:*

$$\sigma_x^2(g) = \int_{\mathbb{R}} (x-t)^2 |g_{t,\xi}(x)|^2 dx = \int_{\mathbb{R}} x^2 |g(x)|^2 dx, \quad (1)$$

and frequency spread $\sigma_\omega(\hat{g})$:

$$\sigma_\omega^2(\hat{g}) = \frac{1}{2\pi} \int_{\mathbb{R}} (\omega - \xi)^2 |\hat{g}_{t,\xi}(\omega)| d\omega = \frac{1}{2\pi} \int_{\mathbb{R}} \omega^2 |\hat{g}(\omega)| d\omega. \quad (2)$$

Now, $V_g f(t, \xi)$ can be thought of as a measure of the frequency content of f at time t and frequency ξ . To learn more about STFT and its properties, see for instance [10].

2.2 Wavelet Analysis

The wavelet transform is another useful tool for time-frequency analysis and the main interest in this thesis. The STFT's “time-frequency window” $g_{t,\xi}$ is replaced by a “time-scale window” $\psi_{a,b}$, with similar properties, but some important differences.

Definition 5 (Continuous Wavelet Transform) *A function ψ with $\int_{\mathbb{R}} \psi(x) dx = 0$ is called a wavelet. For every f , ψ defines the continuous wavelet transform*

$$\mathcal{W}_\psi f(a, b) = \int_{\mathbb{R}} f(x) \frac{1}{\sqrt{a}} \overline{\psi\left(\frac{x-b}{a}\right)} dx \quad \text{for all } a, b \in \mathbb{R}_+ \times \mathbb{R}, \quad (3)$$

where $\psi_{a,b} = \frac{1}{\sqrt{a}} \psi\left(\frac{x-b}{a}\right)$. The function ψ is the so called mother wavelet. It is chosen to be localized at $x = 0$ and at some $\omega = \omega_0 > 0$ (and/or $\omega = -\omega_0$).

The wavelet function $\psi_{a,b}$ has time spread $\sigma_x(\psi_{a,b})$, and energy spread $\sigma_\omega(\hat{\psi}_{a,b})$ around ω_0/a as follows:

$$\sigma_x^2(\psi_{a,b}) = \int_{\mathbb{R}} x^2 |\psi(x)|^2 dx, \quad (4)$$

$$\sigma_\omega^2(\hat{\psi}_{a,b}) = \frac{1}{2\pi} \int_0^\infty (\omega - \omega_0)^2 |\hat{\psi}(\omega)|^2 d\omega, \quad (5)$$

which are modifications of Equations (1) and (2), respectively. Also, Parseval's formula gives a time-frequency interpretation. Since

$$\mathcal{W}_\psi f(a, b) = \int_{\mathbb{R}} f(x) \psi_{a,b}(x) dx = \frac{1}{2\pi} \int_{\mathbb{R}} \hat{f}(\omega) \hat{\psi}_{a,b}(\omega) d\omega,$$

it can be thought of as a measure of the frequency contents of f at the frequency ω_0/a and time b .

Note that $\hat{\psi}_{a,b}(f) = \sqrt{a} \hat{\psi}(af)$. Thus $\hat{\psi}_{a,b}$ is a dilated (or contracted) copy of $\hat{\psi}$. Changing the *dilation parameter* a , changes the support of $\psi_{a,b}$ in time, and rescales ψ . Changing the translation parameter b , on the other hand, makes $\psi_{a,b}$ change its location. Hence varying (a, b) , $\mathcal{W}_\psi f$ can be computed on the entire time-frequency plane. We observe that small scales correspond to high frequencies. This, and the establishment of the expression in Fourier analysis, is why the notation time-frequency plane is used instead of the for wavelet analysis more natural time-scale plane.

Similarly as the CFT, the WCT is used mainly within the theoretical framework of wavelet analysis, for instance in proofs and derivations. Also, although the obvious problems with a continuous transform in a computerized method, the CWT is used as one of the bearing analysis methods in Paper 2. A modified version of the same idea is used in [6]. Another recent Swedish project involving wavelet methods is [17], where wavelets are combined with the Radon transform in the field of local tomography.

For more detailed information about the continuous wavelet transform and its different applications in mathematical analysis, see for instance [12].

2.3 Uncertainty Principles

The wavelet functions are localized both in time and frequency, but it can not be an *exact* localization due to Heisenberg's uncertainty principle. Instead of exact localization, the function is restricted to a so called wavelet Heisenberg box.

The localization measures $\sigma_x(\psi_{a,b})$ and $\sigma_\omega(\hat{\psi}_{a,b})$ are often illustrated as the sides of such rectangles, boxes, in the time-frequency plane. See Figure 2.3 for

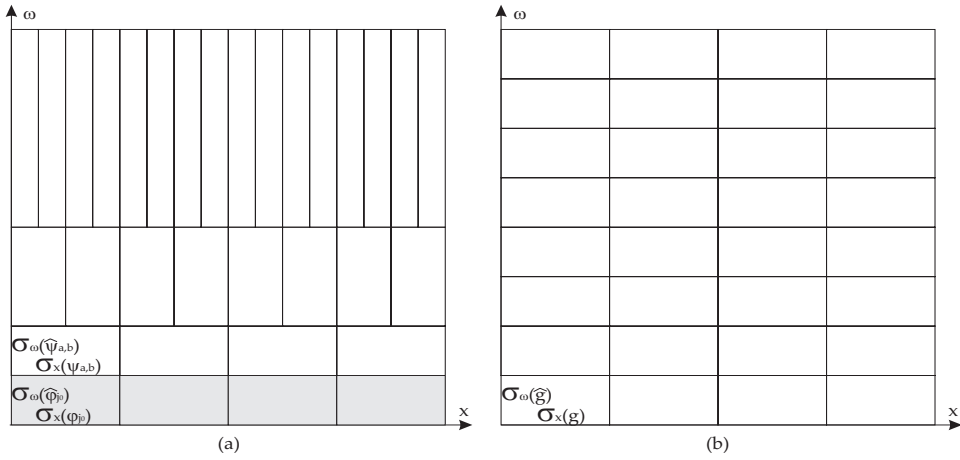


Figure 2: Some adjacent Heisenberg boxes of (a) wavelets $\psi_{a,b}$ and (b) STFT windows $g_{t,\xi}$ with different a , b , t and ξ .

an example. These boxes all have the same area, but their sides are stretched and contracted by the same factors, a and a^{-1} , as the corresponding wavelet functions. The wavelet transform has higher time resolution at higher frequencies and this makes the wavelet transform useful for analysis of signals that contain both low frequencies and short (high frequency) transients. Related methods like wavelet packets and the best basis algorithm (see Section 2.5) can be used to obtain the scheme of Heisenberg box shapes optimal (in some sense) for the application at hand.

The STFT's localization measures $\sigma_x(g)$ and $\sigma_\omega(\hat{g})$ represent the sides of a STFT Heisenberg box. The size of such a box is independent of (t, ξ) , hence the STFT has the same resolution across the entire time-frequency plane. This is visualized in Figure 2.3.

Theorem 1 (Heisenberg's uncertainty principle) *The Heisenberg inequality*

$$\left(\int_{\mathbb{R}} (x - x_0)^2 |f(x)|^2 dx \right)^{\frac{1}{2}} \left(\int_{\mathbb{R}} (\omega - \omega_0)^2 |\hat{f}(\omega)|^2 d\omega \right)^{\frac{1}{2}} \geq \sqrt{\frac{\pi}{2}} \|f\|^2 \quad (6)$$

holds for a function f and for all $x_0, \omega_0 \in \mathbb{R}$. Equality holds if and only if f is a multiple of the (modulated) Gaussian function $e^{i2\pi\omega_0(x-x_0)} e^{-\pi \frac{(x-x_0)^2}{c}}$ for some $\omega_0, x_0 \in \mathbb{R}$ and $c > 0$.

Proof. See, for example, [1, 2]. ■

2.4 Discrete Wavelet Transform

Under certain restrictions on the mother wavelet ψ , all information about the transformed signal is preserved when the wavelet transform is sampled on certain discrete subsets of the time-frequency plane. More precisely, the values of the continuous transform in these points are the coefficients of a corresponding *wavelet basis* series expansion.

Now, return to the CWT and consider the case $a = 2^{-j}$, $b = 2^{-j}k$, where $j, k \in \mathbb{Z}$. Then we get

$$\psi_{2^{-j}, 2^{-j}k}(x) = \frac{1}{\sqrt{2^{-j}}} \psi\left(\frac{x - 2^{-j}k}{2^{-j}}\right) = 2^{j/2} \psi(2^j x - k). \quad (7)$$

Let $w_{j,k}$ represent the values of the CWT, the wavelet coefficients, at the coordinates $(2^{-j}k, 2^{-j})$ representing a dyadic grid in the time-scale plane. The values correspond to the correlation between f and $\psi_{a,b}$ at specific points (a, b) . This “sampling” keeps enough information to make a perfect reconstruction of the signal possible if some special conditions on the wavelet function are fulfilled [3, 8]. If, in addition, even more conditions on ψ are fulfilled, then it turns out that it is possible to construct a function ψ such that $(\psi_{j,k})_{j,k}$ forms an orthonormal basis. This concept leads to what is called the Discrete Wavelet Transform, (DWT).

The first one to construct a smooth wavelet basis was Strömberg [19], who has now been followed by several others e.g. Daubechies [8] and Meyer [16].

Doing a wavelet decomposition with orthonormal wavelet basis functions of a function f yields

$$f = \sum_{j,k} w_{j,k} \psi_{j,k}, \quad (8)$$

where

$$w_{j,k} = \langle f, \psi_{j,k} \rangle. \quad (9)$$

This is a doubly infinite sum over both the time index k and the scale index j . However, the sum can be made finite with little or no error (see e.g. [5]). The case with finitely supported wavelets is clear and for infinitely supported wavelets the main energy should still be concentrated within a certain interval, thus finite summation over k is valid with some approximation.

To understand why finite summation over j is valid, with some approximation, we introduce the concept *Multiresolution Analysis*, (MRA). The MRA, developed by Mallat and Meyer [14, 15], gives the theoretic ground for construction of most wavelets, see for instance [11].

Definition 6 (Multiresolution Analysis) A multiresolution analysis is a family of closed subspaces $V_j \subset L^2(\mathbb{R})$ with the following properties

$$V_j \subset V_{j+1}, \forall j \in \mathbb{Z} \quad (10a)$$

$$f(x) \in V_j \iff f(2x) \in V_{j+1}, \forall j \in \mathbb{Z} \quad (10b)$$

$$\overline{\bigcup_{j \in \mathbb{Z}} V_j} = L^2(\mathbb{R}) \quad (10c)$$

$$\bigcap_{j \in \mathbb{Z}} V_j = \{0\} \quad (10d)$$

$$\exists \varphi \in V_0 \text{ such that } (\varphi(x - k))_{k \in \mathbb{Z}} \text{ is an orthonormal basis for } V_0. \quad (10e)$$

The function φ in Equation (10e) is the so called *scaling function* (or sometimes the approximation function). Note that $V_0 = \overline{\text{Span}_k \varphi_k}$, $k \in \mathbb{Z}$, where $\varphi_k(x) = \varphi(x - k)$. The conditions in Equation (10b) and (10e) yields that $(\varphi_{j,k})_{k \in \mathbb{Z}}$ is an orthonormal basis for V_j , where $\varphi_{j,k}(x) = 2^{j/2} \varphi(2^j x - k)$. Also, $V_j = \overline{\text{Span}_k \varphi_{j,k}}$.

Except for the assumptions on φ due to the MRA, it is usually required that the scaling function should be localized in time. Also, it is common to normalize φ and demand $\int \varphi(x) dx = 1$, (see e.g. [3, 11]).

Now, the definition of MRA implies

$$\varphi(x) = 2 \sum_k h_k \varphi(2x - k), \quad (11)$$

which is known as the *scaling equation*.

Now, we investigate the *detail spaces* W_j , where $V_{j+1} = V_j \oplus W_j$. One can prove, see e.g. [13], that there is a function ψ such that $(\psi_{j,k})_k$ is an orthonormal basis of W_j . For instance, $(\psi(\cdot - k))_k$ is an orthonormal basis of W_0 . It also follows that $(\psi_{j,k})_{j,k}$ is an orthonormal basis for $L^2(\mathbb{R})$.

For practical signals that are bandlimited there is a finest scale $j = J$ for which the wavelet coefficients $w_{j,k}$ are negligible small. We conclude that we can write a function $f_J \in V_J$ as $f_J(x) = \sum_k s_{J,k} \varphi_{J,k}(x)$. Similarly, all functions in W_J can be written on the form $d_J(x) = \sum_k w_{J,k} \psi_{J,k}(x)$.

Summing up, we have

$$\begin{aligned} f_J &\in V_J = V_{J-1} \oplus W_{J-1} = V_{J-2} \oplus W_{J-2} \oplus W_{J-1} \\ &= \dots = V_{j_0} \oplus W_{j_0} \oplus W_{j_0+1} \oplus \dots \oplus W_{J-1}, \end{aligned}$$

and we can write

$$\begin{aligned} f_J &= d_{J-1} + d_{J-2} + \dots + d_{j_0} + f_{j_0} \\ &= \sum_{j=j_0}^{J-1} \sum_k w_{j,k} \psi_{j,k} + \sum_k s_{j_0,k} \varphi_{j_0,k}, \quad \forall f_J \in V_J, \end{aligned} \quad (12)$$

where j_0 is the lowest resolution that is chosen to be included in the analysis.

Using the fact that if $\psi \in W_0 \subset V_1$, and that $\varphi(2x - k)$ is an orthonormal basis for V_1 , ψ can be written as

$$\psi(x) = 2 \sum_k g_k \varphi(2x - k), \quad (13)$$

which is called the *wavelet equation*.

The coefficients (h_k) and (g_k) from the scaling and wavelet equations (11) and (13) work as low pass (approximations), and high pass (details) filters, respectively. These filters are used in the fast filter bank algorithm called *Mallat's algorithm*, see [13]. The DWT of a length- N signal requires $O(N)$ operations using Mallat's algorithm, even less than the FFT which requires $O(N \ln N)$.

We will now briefly explain the DWT algorithm such as it is implemented in a computer program:

Initiation Project the signal on V_J , where J is determined by the sampling frequency. It is common practice to do this simply by replacing the scaling coefficients with the sample values.

- (i) Divide the approximation coefficients into an approximation and a detail part by use of (h_k) and (g_k) .
- (ii) Rescale the approximation coefficients.
- (iii) Process the approximation part again into a new approximation and detail part.
- (iv) Iterate (ii) and (iii) until a satisfactory result is obtained.

Schematically this algorithm can be illustrated by the so called *wavelet tree*, see Figure 3.

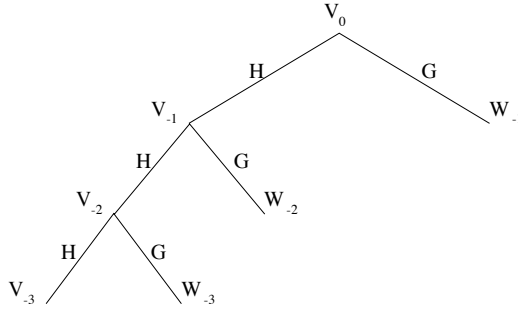


Figure 3: Schematic representation of the discrete wavelet transform, where (g_k) is substituted by G, and (h_k) by H. In this example we have $J = 0$ and $j_0 = -3$.

2.5 Wavelet Packets

Wavelet packets is a natural extension of wavelets that leads to better frequency localization for high frequencies. The same filter functions as in the DWT, (h_k) and (g_k) , are used but now in every possible combination. The corresponding wavelet packet basis functions are defined as $\psi_{j,k,l}(x) = \psi_{j,k,l}(x - 2^{-j}l)|_k$, where k marks the node and l which basis function we have within the node. Similar to the case of wavelet bases, $W_{j,k} = \overline{\text{Span}_l \psi_{j,k,l}}$, and

$$W_{j,k} = W_{j-1,2k} \oplus W_{j-1,2k+1}.$$

Dividing every $\psi_{j,k,l}$ into its low- and high frequency parts gives the schematic picture of a full binary tree. However, in practice the frequency localization of the wavelet packets is not arranged as indicated by the indices, see [16, page 98] or [13, pages 324–327]. It can be realized (for instance experimentally) that each time a high pass filter is passed, the frequency localization will be reversed in relation to the previous order. To calculate a full binary tree requires $O(N \ln N)$ operations, i.e. in level with the FFT.

Although, at each level in the wavelet packet tree we have a full basis and every node $W_{j,k}$ has the relationship $W_{j,k} = W_{j-1,2k} \oplus W_{j-1,2k+1}$ to its children nodes.

2.5.1 Best Basis

The relation $W_{j,k} = W_{j-1,2k} \oplus W_{j-1,2k+1}$ between a parent node and its children nodes makes it possible to choose either basis that cover the frequency plane. We call the collection of all wavelet packet bases possible a *dictionary* of bases. There are at least $2^{2^{J-1}}$ different wavelet packet bases in a full binary tree [13], i.e. a

binary tree of depth J if the signal has length 2^J . Of course the wavelet basis is a special case of the wavelet packet bases.

A certain basis can not be said to be the *best* for all cases but there are ways to find out which basis to choose in a particular case. For this reason there is a value assigned to each node connected to some *cost function*. This function should be additive to make the best basis algorithm cheap.

For different applications, different cost functions should preferably be applied. One of the “standard” cost functions that may be used when the application strives to get only a few large coefficients to represent the signal $c = (c_k)_k$, is the Shannon entropy:

$$H(c) = 2 \log \|c\| - \frac{1}{\|c\|^2} \sum_k |c_k|^2 \log |c_k|^2, \quad \text{where } \|c\|^2 = \sum_k |c_k|^2.$$

Denoising requires a cost function that minimizes the error between the real signal and the denoised signal. One possible choice is the SURE cost function, see [3].

For classification purposes, yet another cost function must be introduced. Then the task is to maximize the discrimination between a number of signals (or classes of signals). Hence, for an optimal choice of basis, every type of application need its own cost function.

In Paper 2 wavelet packets and best basis is mentioned, but without a cost function for loaded bearings at hand, the method is not chosen for further analysis. The basic idea about adaptive time-frequency resolution is used also for Local Discriminant Bases, (LDB). This concept was also briefly covered in Paper 2, and a modified version in [7].

2.6 Final Remarks on Applications

Wavelet based methods, e.g. signal and image processing such as noise reduction, compression, object detection have been proven to be extremely useful for a number of applications such as fingerprint compression, speech recognition and diagnosis of anything from heart trouble to bearing defects. Some other fields where wavelet methods have been used are: approximation theory, numerical analysis, computer science, electrical engineering, physics etc.

In this introduction we have mentioned a number of fairly new applications in connection to this thesis. Moreover, in Paper 2 we have presented a new application, namely *automatic detection of local bearing defects in rotating machines*, which is taken into account when the analysis tool that is used in the industry is implemented.

Bibliography

- [1] G. Bachman, L. Narici, and E. Beckenstein. *Fourier and Wavelet Analysis*. Springer-Verlag New York, 1999.
- [2] J. J. Bendetto and M. W. Frazier, editors. *Wavelets: Mathematics and Applications*. CRC Press, USA, 1994.
- [3] J. Bergh, F. Ekstedt, and M. Lindberg. *Wavelets*. Studentlitteratur, 1999.
- [4] A. Boggess and F. J. Narcowich. *A First Course in Wavelets with Fourier Analysis*. Prentice Hall, Upper Saddle River, New Jersey 07458, 2001.
- [5] C. S. Burrus, R. A. Gopinath, and H. Guo. *Introduction to Wavelets and Wavelet Transforms: A Primer*. Prentice Hall, Upper Saddle River, New Jersey 07458, 1998.
- [6] H. Carlqvist, V. V. Nikulin, J.O. Strömberg, and T. Brismar. Amplitude and phase relationship between alpha and beta oscillations in human EEG. Research report, Department of Mathematics, Royal Institute of Technology, 2004.
- [7] H. Carlqvist, R. Sundberg, and J. O. Strömberg. Separation between classes of multidimensional signals with an improved local discriminant basis algorithm. Research report, Department of Mathematics, Royal Institute of Technology, 2004.
- [8] I. Daubechies. *Ten Lectures on Wavelets*. SIAM, Philadelphia, Pennsylvania, 1992.
- [9] N. Grip. *Wavelet and Gabor Frames and Bases: Approximation, Sampling and Applications*. PhD thesis, Department of Mathematics, Luleå University of Technology, 2002.
- [10] K. Gröchenig. *Foundations of Time-Frequency Analysis*. Applied and Numerical Harmonic Analysis. Birkhäuser, Boston, 2001.
- [11] E. Hernández and G. Weiss. *A First Course on Wavelets*. CRC Press, Florida, USA, 1996.
- [12] M. Holschneider. *Wavelets - An Analysis Tool*. Oxford University Press, New York, USA, 1995.
- [13] S. Mallat. *A Wavelet Tour of Signal Processing*. Academic Press, London, second edition, 1999.

- [14] S. G. Mallat. Multiresolution approximations and wavelet orthohormal bases of $L^2(\mathbb{R})$. *Trans. Amer. Math. Soc.*, 315(1):69–87, Sept 1989.
- [15] Y. Meyer. Ondelettes, fonctions splines et analyses graduées. Lectures given at the University of Torino, Italy, 1986.
- [16] Y. Meyer. *Wavelets and Operators*. Cambridge University Press, Cambridge, UK, 1992.
- [17] M. Nilsson. Local tomography at a glance. Licentiate Thesis, Centre for Mathematical Sciences, Lund Institute of Technology, 2003.
- [18] A. V. Oppenheim, A. S. Willsky, and S. H. Nawab. *Signals & Systems*. Prentice Hall Signal Processing Series. Prentice Hall, Upper Saddle River, New Jersey 07458, second edition, 1997.
- [19] J.O. Strömberg. *A modified Franklin system and higher-order spline systems on \mathbb{R}^n as unconditional bases for Hardy spaces.*, volume 2 of *Conference on harmonic analysis in honor of Antoni Zygmund*. Wadsworth international group, 1983.

Papers

Sampling in Shift-Invariant Spaces

E. Johansson, “Sampling in Shift-Invariant Spaces”.

Sampling in Shift-Invariant Spaces

E. Johansson *

Abstract

This paper deals with sampling in shift-invariant spaces. In particular, we consider irregular sampling, at $\lambda_k = k + \delta_k$, $|\delta_k| < \delta$, in the space V , which is the L_p ($1 \leq p < \infty$) closed span of $\varphi_k = \varphi(\cdot - k)$, where φ belongs to the Wiener amalgam space $W(C, l_1)$. Interpolation is used to estimate the $B(l_p)$ -norm from the $B(l_1)$ - and $B(l_\infty)$ -norm. An example of a family of functions φ_β is worked through. First, the sufficient theoretical demands are confirmed. Then, for the parameters p and β , the maximum jitter error δ , with preserved properties for φ_β , is estimated.

AMS (2000) Subject Classification Primary: 94A20;

Secondary: 42C15, 42C40, 46E22, 47B32.

Key Words and Phrases shift-invariant space, wavelets, irregular sampling, interpolation, reproducing kernel Hilbert space.

1 Introduction

Signals with origin in some physical application, for instance sounds and images, are typically continuous. But, any signal that is to be processed by some sort of computer needs to be a series of discrete values. Hence, if a continuous signal f is to be analyzed by a computer, then it must first be sampled. The sampling procedure generates a set of discrete values $(f(k))_{k \in \mathbb{Z}}$, but there are infinitely many signals with the same sample values and in general it is impossible to recover the original signal from its samples since the behavior between the samples is unknown. In particular, if the signal is band-limited, that is, if its frequency content is confined to $[-\omega_m, \omega_m]$, where ω_m is the maximum frequency of the signal, and also if the sampling frequency $\omega_s \geq 2\omega_m$ according to the Nyquist criteria, then the requirements of the Shannon-Whittaker sampling theorem are fulfilled, see e.g. [3, 7, 16, 17], and we can recover the original signal.

*Department of Mathematics, Luleå University of Technology, Luleå, Sweden

Example 1 (Shannon-Whittaker) *If $f \in L_2$ and $\text{supp}(\hat{f}) \subset [-\pi, \pi]$, then f can be recovered from the samples $\{f(k)\}_{k \in \mathbb{Z}}$ by*

$$f(x) = \sum_{k \in \mathbb{Z}} f(k) \text{sinc}(x - k),$$

where the sampling function

$$\text{sinc}(x) = \begin{cases} \frac{\sin(\pi x)}{\pi x}, & \text{if } x \neq 0 \\ 1, & \text{if } x = 0 \end{cases}.$$

Remark 1 *The sinc function is a very good theoretical example of a sampling function, but it decays slow as $|x| \rightarrow \infty$. This turns out to be a bad property in many practical applications, when numerical implementations are necessary.*

For theoretical aspects one can assume regular sampling, i.e., sampling with a fix time slot between two consecutive samples. Regular sampling is considered in any basic signal processing book, see e.g. [9, 16]. In reality, however, there are almost always errors, for instance due to imperfect clocks, the so called jitter error. This leads to irregular sampling, where the sampling points are given by $\lambda_k = k + \delta_k$, $k \in \mathbb{Z}$. The case when $|\delta_k| < \delta$ is considered in Section 4. Theory for this kind of irregular sampling has been developed in for instance [2, 10, 11, 19]. The purpose of this paper is to study sampling in shift-invariant spaces, which are built up by basis functions that are shifted copies of one function.

Most other papers concerning sampling in shift-invariant spaces, i.e. [1, 2, 19], are thoroughly theoretical, but does not include that many examples. However, with our approach, it is rather easy to transfer theory to practice and implement some examples.

This paper is organized as follows. Section 2 contains general theory that is needed in the rest of the paper. This is followed by a thorough introduction to regular sampling in Section 3 and irregular sampling in Section 4, both focusing on the L_2 case. Then, Section 5 deals with the generalization to L_p , $1 \leq p < \infty$, of the theory concerning the sampling problem. Finally, in Section 6, an example is given where we choose one specific family of sampling functions, check that it has the required theoretical properties, and perform calculations to determine the maximum jitter error δ that makes reconstruction possible.

2 General Theory and Notations

In this section some general theory, on which this paper depends, will be presented. Everything is, in some sense, well known, but we include it for the sake of completeness.

We will mainly operate in the Lebesgue spaces on \mathbb{R} and \mathbb{Z} . Recall that $L_p(\mathbb{R})$, $1 \leq p < \infty$, are spaces of complex-valued Lebesgue measurable functions, f , for which

$$\|f\|_{L_p(\mathbb{R})} = \left(\int_{\mathbb{R}} |f(x)|^p dx \right)^{1/p} < \infty,$$

and that $l_p(\mathbb{Z})$ are the doubly infinite sequences, $a = (a_n)_{n \in \mathbb{Z}}$ of complex numbers such that

$$\|a\|_{l_p(\mathbb{Z})} = \left(\sum_{n \in \mathbb{Z}} |a_n|^p \right)^{1/p} < \infty.$$

The spaces L_∞ and l_∞ are defined analogously, where the integral or sum is replaced by a certain supremum. In order to get simpler notations we will denote these spaces L_p and l_p , and the norms for both cases $\|\cdot\|_p$, whenever it is clear from the context which norm we are referring to. The spaces L_p and l_p are all Banach spaces, and sequences $(f_k)_{k \in \mathbb{Z}}$ in l_p are denoted by either f , (f_k) or $(f_k)_{k \in \mathbb{Z}}$. The elements of L_p are really equivalence classes of functions under the relation $f = g$ if $\|f - g\|_p = 0$, i.e., they are equal almost everywhere. When we talk about a continuous function f in L_p , what we really mean is the continuous representative of f .

As the Fourier transform of $f \in L_1$ we use

$$\hat{f}(\omega) = \int_{\mathbb{R}} f(x) e^{-i\omega x} dx,$$

and with the usual extension for functions in L_2 .

Given two Banach spaces X and Y , we use $B(X, Y)$ to denote the space of bounded linear functions from X to Y . The space $B(X, Y)$ is a Banach space equipped with the norm

$$\|T\|_{B(X, Y)} = \sup_{\|f\|_X \leq 1} \|Tf\|_Y.$$

Of special interest for us is the subspace $G(X, Y)$ of $B(X, Y)$, consisting of the bijective operators in $B(X, Y)$. Hence, if $T \in G(X, Y)$ we can define its inverse T^{-1} , which will belong to $G(Y, X)$, via the open mapping theorem. If $X = Y$ we simply denote these by $B(X)$ and $G(X)$, respectively.

When considering sampling, the Wiener amalgam spaces occur naturally. We will use the spaces $W(C, l_p)$ which are the continuous functions f from \mathbb{R} to \mathbb{C} equipped with the norm

$$\|f\|_{W(C, l_p)} = \left(\sum_{n \in \mathbb{Z}} \sup_{0 \leq x \leq 1} |f(n+x)|^p \right)^{1/p},$$

see [12], which turns out to be a Banach space.

Before we proceed towards more sampling related theory, we need the concept of Riesz bases. Let $(f_k)_{k \in \mathbb{Z}}$ be a sequence in L_2 and V be the closed linear span of (f_k) . Then (f_k) is said to be a Riesz basis for V if there are two positive constants A and B such that

$$A \|a\|_2 \leq \left\| \sum_k a_k f_k \right\|_2 \leq B \|a\|_2, \quad (1)$$

for sequences $a \in l_2$ for which only a finite number of entries are nonzero. Note that Equation (1) ensures numerical stability since a small change in a results in a small change in $\sum_k a_k \varphi_k$ and vice versa.

Let (e_k) be the standard basis of l_2 and define the operator $T_{(f_i)}$ in such a way that it maps e_k on f_k , i.e., $T_{(f_i)} a = \sum_k a_k f_k$. Then the condition in Equation (1) can be reformulated as: $T_{(f_i)}$ is an element in $G(l_2, V)$. We call $T_{(f_i)}$ the synthesis mapping for (f_k) and its inverse $T_{(f_i)}^{-1}$ the analysis mapping. Now, define $\tilde{f}_j = (T_{(f_i)}^{-1})^* e_j$, $(T_{(f_i)}^{-1})^* \in G(V, l_2)$, which is another Riesz basis for V . It is dual to (f_k) in the sense that: $\langle f_k, \tilde{f}_j \rangle = \langle T_{(f_i)} e_k, T_{(f_i)}^{-1*} e_j \rangle = \langle e_k, e_j \rangle = \delta_{kj}$, where δ_{kj} is the Kronecker delta function that is one if $j = k$ and zero otherwise. Moreover, we get the following expansions

$$\begin{aligned} f &= T_{(f_i)} T_{(f_i)}^{-1} f = T_{(f_i)} \sum_k \langle T_{(f_i)}^{-1} f, e_k \rangle e_k \\ &= \sum_k \langle f, (T_{(f_i)}^{-1})^* e_k \rangle T_{(f_i)} e_k = \sum_k \langle f, \tilde{f}_k \rangle f_k \end{aligned}$$

and

$$\begin{aligned} f &= (T_{(f_i)}^*)^{-1} T_{(f_i)}^* f = (T_{(f_i)}^*)^{-1} \sum_k \langle T_{(f_i)}^* f, e_k \rangle e_k \\ &= \sum_k \langle f, T_{(f_i)} e_k \rangle (T_{(f_i)}^{-1})^* e_k = \sum_k \langle f, f_k \rangle \tilde{f}_k. \end{aligned}$$

We say that V is a shift-invariant space generated by $\varphi_k = \varphi(\cdot - k)$ if it is the L_2 -closed linear span of the sequence (φ_k) . We will assume that $\varphi \in W(C, l_1)$, since the Wiener amalgam spaces supply a framework for pointwise evaluation which is essential in sampling theory. Furthermore, we assume that $(\varphi_k)_{k \in \mathbb{Z}}$ is a Riesz basis for V . When we have this extra property it holds that: (φ_k) is a Riesz basis for V if there are two positive and finite constants A and B such that

$$A \leq \sum_k |\hat{\varphi}(\omega + 2\pi k)|^2 \leq B \quad \text{a.e.}$$

For more on Riesz bases see e.g. [6, 12, 22, 23]. It is shown in [10] that, with the above conditions on φ , if $g_n \rightarrow g$ in V , then $g_n \rightarrow g$ uniformly on \mathbb{R} .

A main example of shift invariant space is the space V_0 of an MRA occurring in the theory of wavelets, see e.g. [3, 5, 8, 13–15].

It will be shown in Section 3 that the shift invariant space of interest V , generated by φ_k , is a reproducing kernel Hilbert space. This means that the functional

$$f \mapsto f(x),$$

where x is fixed, belongs to $B(V, \mathbb{C})$, and hence there exists, by the Riesz representation theorem, $K_x \in V$ such that

$$f(x) = \langle f, K_x \rangle.$$

This function K_x is called the reproducing kernel.

In what follows we will have to show that a particular operator $T \in B(X)$ is invertible, i.e., $T \in G(X)$, and this will be done by the following:

An operator $T \in B(X)$ is invertible if and only if there exists $\Lambda \in G(X)$ such that

$$\|I - \Lambda T\|_{B(X)} < 1, \quad (2)$$

where I denotes the identity mapping.

The “if” direction follows by the observation that $\sum_{k=0}^{\infty} (I - \Lambda T)^k$ converges to $(\Lambda T)^{-1}$ and since Λ is invertible, so is T , and the “only if” follows by choosing $\Lambda = T^{-1}$. So, our strategy will be to find a suitable invertible operator Λ and show that the norm of $I - \Lambda T$ is less than one. However, estimating norms is a tough task. Here we will do it by using interpolation. In our case the space X will be l_p and we will have an operator $S : l_p \rightarrow l_p$. The operator can be represented by elements s_{ij} , $i, j \in \mathbb{Z}$, of complex numbers such that: $(Sa)_i = \sum_j s_{ij} a_j$. The norm of such an operator can be estimated with help of the following theorem.

Theorem 1 *Let $A = \sup_j \sum_i |s_{ij}|$ and $B = \sup_i \sum_j |s_{ij}|$. If A and B are finite, then $S \in B(l_p)$ and with the norm estimate $\|S\|_{B(l_p)} \leq A^{1/p} B^{1/p'}$, where $1/p + 1/p' = 1$, and $1 \leq p \leq \infty$.*

This theorem is due to Schur, see [18], and it is a special case of general interpolation theory, see [4]. We now present an elementary proof of this theorem:

Proof. We know that

$$\|S\|_{B(l_p)} = \sup_{\|a\|_p=1} \|Sa\|_p,$$

where

$$\|Sa\|_p = \left(\sum_i \left| \sum_j s_{ij} a_j \right|^p \right)^{1/p}.$$

First,

$$\left| \sum_j s_{ij} a_j \right|^p \leq \left(\sum_j |s_{ij} a_j| \right)^p,$$

due to the triangle inequality. Now

$$\begin{aligned} \sum_j |s_{ij} a_j| &= \sum_j |s_{ij}|^{1/p} |a_j| |s_{ij}|^{1/p'} \\ &\leq \left(\sum_j |s_{ij}| |a_j|^p \right)^{1/p} \left(\sum_j |s_{ij}| \right)^{1/p'}, \end{aligned}$$

by Hölder's inequality, and

$$\begin{aligned} \|Sa\|_p^p &= \sum_i \left(\sum_j |s_{ij}| |a_j|^p \left(\sum_j |s_{ij}| \right)^{p/p'} \right) \\ &\leq \sum_i \sum_j |s_{ij}| |a_j|^p \left(\sup_i \sum_j |s_{ij}| \right)^{p/p'} = B^{p/p'} \sum_j |a_j|^p \sum_i |s_{ij}| \\ &\leq B^{p/p'} \sup_j \sum_i |s_{ij}| \sum_j |a_j|^p = AB^{p/p'} \|a\|_p^p. \end{aligned}$$

Finally

$$\|S\|_{B(lp)} = \sup_{\|a\|_p=1} \|Sa\|_p \leq A^{1/p} B^{1/p'}. \quad (3)$$

The proof is complete. ■

The numbers A and B are the norms in $B(l_1)$ and $B(l_\infty)$ respectively, hence Equation (3) may be rewritten as

$$\|S\|_{B(lp)} \leq \|S\|_{B(l_1)}^{1/p} \|S\|_{B(l_\infty)}^{1/p'}. \quad (4)$$

3 Regular Sampling

Consider a function $f, f \in V \subset L_2$, where V is a shift-invariant space, generated by the Riesz basis $(\varphi_k)_{k \in \mathbb{Z}}$, which has a dual basis $(\widetilde{\varphi}_k)_{k \in \mathbb{Z}}$, and $\varphi \in W(C, l_1)$. We know that we can write f as

$$f = \sum_{k \in \mathbb{Z}} \langle f, \widetilde{\varphi}_k \rangle \varphi_k = \sum_{k \in \mathbb{Z}} \langle f, \varphi_k \rangle \widetilde{\varphi}_k. \quad (5)$$

Now, we are looking for an expression for f as the following:

$$f = \sum_{k \in \mathbb{Z}} f(k) \widetilde{q}_k, \quad (6)$$

where $(f(k))_k$ is the sequence of sampled values from the function f and q_k, \widetilde{q}_k is some Riesz basis and its dual. Note that $f(k)$ is well defined since V consists of continuous functions. Hence, what we need is that

$$f(k) = \langle f, q_k \rangle, \quad (7)$$

i.e., we need to show that the reproducing kernel gives a Riesz basis. Since convergence in V implies uniform convergence, we can use Equation (5) and get

$$f(x) = \sum_{k \in \mathbb{Z}} \langle f, \widetilde{\varphi}_k \rangle \varphi_k(x) = \sum_{k \in \mathbb{Z}} \langle f, \widetilde{\varphi}_k \bar{\varphi}_k(x) \rangle = \langle f, \sum_{k \in \mathbb{Z}} \widetilde{\varphi}_k \bar{\varphi}_k(x) \rangle, \quad (8)$$

where the sum in the last expression converges in l_2 since $\bar{\varphi}_k(x) \in l_2$. Hence, if we let

$$q_x = \sum_{k \in \mathbb{Z}} \widetilde{\varphi}_k \bar{\varphi}_k(x), \quad (9)$$

we see that q_x is the reproducing kernel that we were looking for. Now, we have to find conditions for when (q_k) is a Riesz basis for V , i.e., to check when $T_{(q_i)} \in G(l_2, V)$. For this purpose we define Γ , a linear operator that maps φ_k on q_k . Then $T_{(q_i)} = \Gamma \circ T_{(\varphi_i)}$ and it comes down to check when $\Gamma \in G(V)$. Let $\Phi \in B(l_2)$ be the operator $\Phi a = \sum_{j \in \mathbb{Z}} \bar{\varphi}_k(j) a_j$. We write $\Phi = [\bar{\varphi}_k(j)] = [\bar{\varphi}(j - k)]$ or $\Phi_{jk} = \bar{\varphi}_k(j)$. Applying Γ on f , where $f = \sum a_j \varphi_j$ with only a finite number of nonzero terms, we get

$$\begin{aligned} \Gamma f &= \sum_{k \in \mathbb{Z}} \langle \Gamma f, \varphi_k \rangle \widetilde{\varphi}_k = \sum_{k \in \mathbb{Z}} \langle \Gamma \sum_{j \in \mathbb{Z}} a_j \varphi_j, \varphi_k \rangle \widetilde{\varphi}_k \\ &= \sum_{k \in \mathbb{Z}} \langle \sum_{j \in \mathbb{Z}} a_j \Gamma \varphi_j, \varphi_k \rangle \widetilde{\varphi}_k = \sum_{k \in \mathbb{Z}} (\sum_{j \in \mathbb{Z}} \langle q_j, \varphi_k \rangle a_j) \widetilde{\varphi}_k \\ &= \sum_{k \in \mathbb{Z}} (\sum_{j \in \mathbb{Z}} \overline{\varphi_k(j)} a_j) \widetilde{\varphi}_k = T_{(\widetilde{\varphi}_i)} (\sum_{j \in \mathbb{Z}} \overline{\varphi_k(j)} a_j)_k \\ &= T_{(\widetilde{\varphi}_i)} \Phi a = T_{(\widetilde{\varphi}_i)} \Phi T_{(\varphi_i)}^{-1} f, \end{aligned}$$

i.e., $\Gamma = T_{(\bar{\varphi}_i)} \Phi T_{(\varphi_i)}^{-1}$ on a dense subset of V . The operators $T_{(\bar{\varphi}_i)}$ and $T_{(\varphi_i)}^{-1}$ are in $G(l_2, V)$ and $G(V, l_2)$, respectively, thus $\Gamma \in G(V)$ if and only if $\Phi \in G(l_2)$. Hence (q_k) is a Riesz basis if $\Phi \in G(l_2)$. To verify this we check the sufficient condition $\|I - \Lambda\Phi\| < 1$ for a particular $\Lambda \in G(l_2)$.

To estimate the l_2 -norm we will use the results of the Schur interpolation described in Section 2 and an operator $\Lambda \in G(l_2)$. In this case we have chosen $\Lambda = 1/\bar{\varphi}(0) I$, which may be interpreted as a normalization of Φ . Now let the elements in $I - \Lambda\Phi$ be illustrated as the elements in a doubly infinite matrix. We get the norms $\|I - \Lambda\Phi\|_{B(l_1)} = \|I - \Lambda\Phi\|_{B(l_\infty)}$, corresponding to Equation (2), since for every row, there is a column with the same elements. Hence,

$$\|I - \Lambda\Phi\|_{B(l_2)} \leq \|I - \Lambda\Phi\|_{B(l_1)} = \|I - \Lambda\Phi\|_{B(l_\infty)},$$

when

$$I - \Lambda\Phi = \frac{1}{\bar{\varphi}(0)} \begin{bmatrix} \ddots & \ddots & \ddots & & & \\ \ddots & 0 & -\bar{\varphi}(1) & -\bar{\varphi}(2) & & \\ \ddots & -\bar{\varphi}(-1) & \ddots & \ddots & -\bar{\varphi}(2) & \\ & -\bar{\varphi}(-2) & \ddots & \ddots & -\bar{\varphi}(1) & \ddots \\ & & -\bar{\varphi}(-2) & -\bar{\varphi}(-1) & 0 & \ddots \\ & & & \ddots & \ddots & \ddots \end{bmatrix}, \quad (10)$$

and

$$\|I - \Lambda\Phi\|_{B(l_1)} = \|I - \Lambda\Phi\|_{B(l_\infty)} = \sum_{k \neq 0} |\varphi(k)| / |\varphi(0)|.$$

To fulfill the requirements in Equation (2), via Equation (3), what we need is that $\sum_{k \neq 0} |\varphi(k)| / |\varphi(0)| < 1$, i.e., $\sum_{k \neq 0} |\varphi(k)| < |\varphi(0)|$. Note that choosing $\Lambda = I$ gives a similar matrix but without the factor $1/\bar{\varphi}(0)$ and with all diagonal elements equal to $1 - \bar{\varphi}(0)$. Calculating the norms gives

$$\|I - \Phi\|_{B(l_1)} = \|I - \Phi\|_{B(l_\infty)} = \sum_{k \neq 0} |\varphi(k)| + |1 - \bar{\varphi}(0)|,$$

which yields the previous if $0 \leq \bar{\varphi}(0) \leq 1$.

4 Irregular Sampling

Due to for instance imperfect clocks we might have small errors in the sampling points, jitter errors, which make the sampling irregular. The sampling points are

now given by $\lambda_k = k + \delta_k$, $k \in \mathbb{Z}$, where the errors δ_k have the property $\sup_{k \in \mathbb{Z}} |\delta_k| < \delta \leq 1/2$. It is necessary that $\delta \leq 1/2$ if the sampling is supposed to be at the integers, since $\delta > 1/2$ might result in confusion about the order of the samples. The Riesz basis that generates the shift-invariant space V is still $(\varphi_k)_{k \in \mathbb{Z}}$, with dual basis $(\tilde{\varphi}_k)_{k \in \mathbb{Z}}$, and for a function $f \in V \subset L_2$ we have

$$f = \sum_{k \in \mathbb{Z}} \langle f, \varphi_k \rangle \tilde{\varphi}_k.$$

Differences from the regular case are noted when we proceed to the equivalences to Equation (1) and Equation (7), that is $f = \sum_{k \in \mathbb{Z}} f(\lambda_k) \widetilde{q_{\lambda_k}}$ and $f(\lambda_k) = \langle f, q_{\lambda_k} \rangle$ respectively, where $q_{\lambda_k} = \sum_{k \in \mathbb{Z}} \widetilde{\varphi_k} \varphi_k(\lambda_k)$.

It is easy to continue the derivation in the same manner as in Section 3 with k changed to λ_k whenever the sampling points are considered, hence the operator $\Gamma \in G(V)$ now maps φ_k on q_{λ_k} . Applying Γ on f gives

$$\Gamma f = T_{(\widetilde{\varphi_i})} \Phi T_{(\varphi_i)}^{-1} f,$$

where $\Phi = [\widetilde{\varphi_k}(\lambda_j)] = [\widetilde{\varphi}(\lambda_j - k)]$. Now, we proceed with checking the inequality $\|I - \Lambda \Phi\|_{B(l_2)} < 1$, where $\Lambda \in G(l_2)$ is chosen to be $\Lambda_{kk} = 1/\Phi_{kk} = 1/\widetilde{\varphi_k}(\lambda_k) = 1/\widetilde{\varphi}(\delta_k)$, which is comparable to $\Lambda = 1/\widetilde{\varphi}(0)$ in Section 3. In this case, with irregular sampling, the equivalence to Equation (10) is:

$$I - \Lambda \Phi = \begin{bmatrix} \ddots & \ddots & \ddots & & & \\ \ddots & 0 & -\frac{\widetilde{\varphi}(\delta_{-1}-1)}{\widetilde{\varphi}(\delta_{-1})} & -\frac{\widetilde{\varphi}(\delta_{-1}-2)}{\widetilde{\varphi}(\delta_{-1})} & & \\ \ddots & -\frac{\widetilde{\varphi}(\delta_0+1)}{\widetilde{\varphi}(\delta_0)} & \ddots & -\frac{\widetilde{\varphi}(\delta_0-1)}{\widetilde{\varphi}(\delta_0)} & -\frac{\widetilde{\varphi}(\delta_0-2)}{\widetilde{\varphi}(\delta_0)} & \\ & -\frac{\widetilde{\varphi}(\delta_1+2)}{\widetilde{\varphi}(\delta_1)} & -\frac{\widetilde{\varphi}(\delta_1+1)}{\widetilde{\varphi}(\delta_1)} & \ddots & -\frac{\widetilde{\varphi}(\delta_1-1)}{\widetilde{\varphi}(\delta_1)} & \ddots \\ & & -\frac{\widetilde{\varphi}(\delta_2+2)}{\widetilde{\varphi}(\delta_2)} & -\frac{\widetilde{\varphi}(\delta_2+1)}{\widetilde{\varphi}(\delta_2)} & 0 & \ddots \\ & & & \ddots & \ddots & \ddots \end{bmatrix}, \quad (11)$$

hence the norms are

$$\|I - \Lambda \Phi\|_{B(l_1)} = \sup_{k \in \mathbb{Z}} \sum_{j \neq 0} \left| \frac{\varphi(\delta_{j-k} + j)}{\varphi(\delta_{j-k})} \right|, \quad (12)$$

and

$$\|I - \Lambda \Phi\|_{B(l_\infty)} = \sup_{k \in \mathbb{Z}} \sum_{j \neq 0} \left| \frac{\varphi(\delta_k + j)}{\varphi(\delta_k)} \right|. \quad (13)$$

Now, we want Equations (12) and (13) to be valid for any sequence (δ_k) , $|\delta_k| < \delta$, hence we rewrite and estimate the expressions for the norms as:

$$\|I - \Lambda\Phi\|_{B(l_1)} \leq \sum_{j \neq 0} \sup_{|\mu| < \delta} \left| \frac{\varphi(\mu + j)}{\varphi(\mu)} \right| = \sum_{j \neq 0} \sup_{|\mu| < \delta} a_{\mu j}, \quad (14)$$

where $a_{\mu j} = |\varphi(\mu + j) / \varphi(\mu)|$, and

$$\|I - \Lambda\Phi\|_{B(l_\infty)} \leq \sup_{|\mu| < \delta} \sum_{j \neq 0} \left| \frac{\varphi(\mu + j)}{\varphi(\mu)} \right| = \sup_{|\mu| < \delta} \sum_{j \neq 0} a_{\mu j}. \quad (15)$$

Note that, in contrast to the case with regular sampling, the two norms are not equal. In Equation (14) we take the sum of the supremum of a function on each interval $(j - \delta, j + \delta)$, whilst Equation (15) is supremum of the sum of the same function but with fixed error μ . As a consequence, $\|I - \Lambda\Phi\|_{B(l_1)}$, where every term in the sum is maximized, will always be bigger or equal to $\|I - \Lambda\Phi\|_{B(l_\infty)}$, where the whole sum is maximized.

Finally, we may proceed as in Section 3 and get

$$\begin{aligned} \|I - \Lambda\Phi\|_{B(l_2)} &\leq \|I - \Lambda\Phi\|_{B(l_1)}^{1/2} \|I - \Lambda\Phi\|_{B(l_\infty)}^{1/2} \\ &\leq \left(\sum_{j \neq 0} \sup_{|\mu| < \delta} a_{\mu j} \right)^{1/2} \left(\sup_{|\mu| < \delta} \sum_{j \neq 0} a_{\mu j} \right)^{1/2}. \end{aligned} \quad (16)$$

5 Generalization to L_p

In this section we will present our sampling problem in L_p setting, where $1 \leq p < \infty$, and we do so by following the outline in [2].

Riesz bases are usually defined in subspaces of L_2 . They can, however, be defined in much greater generality, see e.g. [6].

We define our shift invariant space V in L_p , $1 \leq p < \infty$, as follows: Let V be the L_p closed linear span of $\varphi_k = \varphi(\cdot - k)$ where $\varphi \in W(C, l_1)$ and we assume that there exists positive and finite constants A and B such that

$$A \|a\|_p \leq \left\| \sum_k a_k \varphi_k \right\|_p \leq B \|a\|_p, \quad (17)$$

holds for sequences $a \in l_p$ for which only a finite number of entries are nonzero. Now, Equation (17) ensures numerical stability and, furthermore, it turns out that φ_k is an unconditional basis for V which is a subspace of $W(C, l_p)$. The condition

in Equation (17) holds if the corresponding condition holds for $p = 2$, and for this it is sufficient to check

$$A \leq \sum_k |\widehat{\varphi}(\omega + 2\pi k)|^2 \leq B, \quad \text{a.e.}, \quad (18)$$

since $\varphi_k(x) = \varphi(x - k)$. So, we assume (18).

To arrive at a sampling result we proceed as follows: Let $f \in V$. Then we have

$$f = \sum_k a_k \varphi_k, \quad (19)$$

with convergence in L_p . In particular, f is continuous and

$$f(x) = \sum_k a_k \varphi(x - k). \quad (20)$$

In the case when $p = 2$ our sampling result is of the type

$$f = \sum_k f(\lambda_k) \widetilde{q_{\lambda_k}},$$

where the sum is a Riesz basis expansion. Now, our sampling result is weaker, it merely says that the sequence $f(\lambda_j)$ determines f uniquely. Given $f(\lambda_j)$, Equation (20) gives

$$f(\lambda_j) = \sum_k a_k \varphi(\lambda_j - k). \quad (21)$$

Denote $(f(\lambda_j))_j = F$, $(a_j)_j = a \in l_p$. Since $f \in V_p \subset W(C, l_p)$ and $|\lambda_j - j| \leq \delta$ it follows that $F \in l_p$. This means that Equation (21) can be seen as

$$F = \Phi a,$$

where Φ is an operator from l_p to l_p and that the operator is given by the elements of a complex matrix $[\varphi(\lambda_j - k)]$, $j, k \in \mathbb{Z}$. So, to determine f from $f(\lambda_j)$ we have to be able to solve this equation for a which gives f from Equation (19), hence it is necessary that the operator Φ is invertible. If so, $a = \Phi^{-1}F$. By plugging this into Equation (19) we get a formal expansion, if Φ^{-1} is represented by b_{jk} in the usual sense;

$$\begin{aligned} f &= \sum_j a_j \varphi_j = \sum_j \sum_k b_{jk} f(\lambda_k) \varphi_j \\ &= \sum_k f(\lambda_k) q_k, \end{aligned}$$

where $q_k = \sum_j b_{jk} \varphi_j$. Our objective is thus to check whether the operator Φ is invertible and as before we do so by checking if we can find $\Lambda \in G(l_p)$ such that $\|I - \Lambda\Phi\|_{B(l_p)} < 1$. To check the norm we will use the interpolation in Equation (3), similar to the case when $p = 2$.

In the following theorem, we summarize the theoretical framework that we have built up in the previous sections.

Theorem 2 (Sampling in Shift-Invariant Spaces) *Let $\varphi \in W(C, l_1)$ such that*

$$0 < A \leq \sum_k |\widehat{\varphi}(\omega + 2\pi k)|^2 \leq B < \infty \quad a.e. \quad (22)$$

Define V , $1 \leq p < \infty$, as the L_p closure of $\{\varphi(\cdot - k)\}_{k \in \mathbb{Z}}$. The sequence $(\varphi(\cdot - k))_{k \in \mathbb{Z}}$ will be an unconditional basis of V , in particular, when $p = 2$, $(\varphi(\cdot - k))_{k \in \mathbb{Z}}$ is a Riesz basis. Furthermore, if

$$\left(\sum_{j \neq 0} \sup_{|\mu| < \delta} \left| \frac{\varphi(\mu + j)}{\varphi(\mu)} \right| \right)^{1/p} \left(\sup_{|\mu| < \delta} \sum_{j \neq 0} \left| \frac{\varphi(\mu + j)}{\varphi(\mu)} \right| \right)^{1/p'} < 1,$$

where $1/p + 1/p' = 1$, then for all sequences $(\delta_k)_{k \in \mathbb{Z}}$ with $|\delta_k| < \delta$, there exists $q_k \in V$ such that

$$f = \sum_k f(\delta_k + k) q_k.$$

If $p = 2$, this is a Riesz expansion and if $p \neq 2$ a formal expansion, and then the conclusion is that the sequence $(f(\delta_k + k))_{k \in \mathbb{Z}}$ determines f uniquely.

6 Example

This section consists mainly of the theory in Section 4 applied to the sampling function given in [20, 21]:

$$\varphi_\beta(x) = \frac{\sin \pi x \cos \pi \beta x}{\pi x (1 - 4(\beta x)^2)}, \quad (23)$$

$0 < \beta < \infty$. The estimations that we use in the calculations of the norms are however valid only for $0 < \beta < 3$.

Note that in this section we use the notation φ_β which does not coincide with the meaning of the previously used φ_k , i.e., $\varphi_\beta \neq \varphi(\cdot - \beta)$. Also note that if we let $\beta \rightarrow 0$ the sampling function converges to $\varphi_0(x) = \text{sinc}(x)$. But $\text{sinc}(x) \notin W(C, l_1)$ and $\sum |\varphi(\lambda_k)| = \infty$, hence the conditions are not satisfied for $\beta = 0$.

There are removable singularities in φ_β at $x = 0$ and at $x = \pm 1/(2\beta)$. We actually define φ_β as the inverse Fourier transform of $1/2\pi$ times the convolution of $\chi_{[-\pi, \pi]}(\omega)$ and $\frac{\pi}{2\beta} \cos \frac{\omega}{2\beta} \chi_{[-\pi\beta, \pi\beta]}(\omega)$, i.e.,

$$\begin{aligned}\hat{\varphi}_\beta(\omega) &= \frac{1}{2\pi} \chi_{[-\pi, \pi]}(\omega) * \frac{\pi}{2\beta} \cos \frac{\omega}{2\beta} \chi_{[-\pi\beta, \pi\beta]}(\omega) \\ &= \frac{1}{2\pi} \int_{\mathbb{R}} \chi_{[-\pi, \pi]}(u - \omega) \frac{\pi}{2\beta} \cos \frac{u}{2\beta} \chi_{[-\pi\beta, \pi\beta]}(u) du \\ &= \frac{1}{2\pi} \int_{\omega - \pi}^{\omega + \pi} \frac{\pi}{2\beta} \cos \frac{u}{2\beta} \chi_{[-\pi\beta, \pi\beta]}(u) du,\end{aligned}$$

and this is Equation (23) with the singularities removed. It is clear that $\hat{\varphi}_\beta(\omega)$ has compact support, hence $\varphi_\beta \in C^\infty$. The Fourier transform, $\hat{\varphi}_\beta$, of the sampling function has support in $[-\pi(1 + \beta), \pi(1 + \beta)]$, is bell-shaped, and when $\beta < 1$ there is a flat section for $|\omega| \leq \pi(1 - \beta)$. Thus, for this example $\hat{\varphi}_\beta(\omega) \leq \hat{\varphi}_\beta(0)$, where

$$\hat{\varphi}_\beta(0) = \begin{cases} \sin\left(\frac{\pi}{2\beta}\right), & \text{if } \beta \geq 1 \\ 1, & \text{if } \beta \leq 1. \end{cases}$$

Moreover,

$$\begin{aligned}|\varphi'_\beta(x)| &= \left| \frac{d}{dx} \frac{1}{2\pi} \int \hat{\varphi}(\omega) e^{i\omega x} d\omega \right| \leq \frac{1}{2\pi} \hat{\varphi}(0) \int |i\omega e^{i\omega x}| d\omega \\ &= \frac{1}{\pi} \int_0^{\pi(1+\beta)} |\omega| d\omega = \frac{\pi}{2} (1 + \beta)^2 < 8\pi,\end{aligned}$$

where the last inequality is due to our restriction that $\beta < 3$. Hence, the derivative of φ_β is bounded and it will for instance be possible to find extreme values with adequate accuracy.

Clearly $\varphi_\beta \in W(C, l_1)$ and we now must verify that $(\varphi_\beta(\cdot - k))$ really is a Riesz basis. This is done via Equation (18). We have

$$\begin{aligned}\sum_k \hat{\varphi}_\beta(\omega + 2\pi k) &= \frac{1}{2\pi} \sum_k \int_{\omega - \pi + 2\pi k}^{\omega + \pi + 2\pi k} \frac{\pi}{2\beta} \cos \frac{u}{2\beta} \chi_{[-\pi\beta, \pi\beta]}(u) du \\ &= \frac{1}{2\pi} \int \frac{\pi}{2\beta} \cos \frac{u}{2\beta} \chi_{[-\pi\beta, \pi\beta]}(u) du = \frac{1}{4\beta} \int_{-\pi\beta}^{\pi\beta} \cos \frac{u}{2\beta} du \\ &= \left[\sin \frac{u}{2\beta} \right]_0^{\pi\beta} = 1,\end{aligned}$$

and since we know that $0 \leq \hat{\varphi}_\beta(\omega) \leq 1$ for every ω , we draw the conclusions that

$$\sum_k \hat{\varphi}_\beta(\omega + 2\pi k) = \sum_k |\hat{\varphi}_\beta(\omega + 2\pi k)| \geq \sum_k |\hat{\varphi}_\beta(\omega + 2\pi k)|^2,$$

thus $B = 1$ in this case. To determine whether there is an $A > 0$ we proceed as follows. Since $\text{supp } \hat{\varphi}_\beta \supset [-\pi, \pi]$, two consecutive translates of $\hat{\varphi}_\beta$, $\hat{\varphi}_\beta(\omega + 2\pi n)$ and $\hat{\varphi}_\beta(\omega + 2\pi(n+1))$, will always overlap, hence

$$|\hat{\varphi}_\beta(\omega + 2\pi k)|^2 \geq |\hat{\varphi}_\beta(\pi)|^2 \geq \begin{cases} \frac{1}{4} \sin^2 \frac{\pi}{\beta}, & \text{if } \beta \in (2, 3) \\ \frac{1}{4}, & \text{if } \beta \leq 2, \end{cases}$$

and there exists clearly a constant $0 < A \leq \sum_k |\hat{\varphi}_\beta(\omega + 2\pi k)|^2$.

In the papers [20, 21], however, the authors' only concern is the case when $\beta < 1/3$. Their goal is to find wavelets in closed form, not general Riesz bases for shift invariant spaces and the upper limit $1/3$ is due to the MRA conditions, see [20]. We will now see why. Given $V_0 = V$, define V_j via $f \in V_j \Leftrightarrow f(2^{-j}\cdot) \in V_0$. The relation

$$\hat{\varphi}_\beta(\omega) = \hat{\varphi}_\beta(\omega/2) \alpha(\omega), \quad (24)$$

where $\alpha(\omega)$ is a 4π -periodic function, implies that $V_j \subset V_{j+1}$ i.e., one of the MRA conditions. Now define a 4π -periodic function $\alpha(\omega)$ as

$$\alpha(\omega) = \begin{cases} \hat{\varphi}_\beta(\omega), & |\omega| \leq \pi(1 + \beta) \\ 0, & \pi(1 + \beta) \leq |\omega| \leq 2\pi, \end{cases}$$

and check if and when Equation (24) is fulfilled. Using the fact that $\hat{\varphi}_\beta(\omega/2) = 1$ for $|\omega| \leq 2\pi(1 - \beta)$, we come down to the conditions $\pi(1 + \beta) \leq 2\pi(1 - \beta)$ and $-\pi(1 + \beta) \geq -2\pi(1 - \beta)$ for Equation (24) to hold. Both inequalities give $\beta \leq 1/3$. By Theorem 1.6 and 1.7, Chapter 2 in [13], we conclude that φ_β generates an MRA when $\beta \leq 1/3$ since $\hat{\varphi}_\beta(0) = 1 \neq 0$.

Now, when we know that $(\varphi_\beta(\cdot - k))$ is a Riesz basis our goal is to estimate the maximum value of δ , the disturbance from regular sampling, that still makes reconstruction possible. This is done by calculating estimations of $\|I - \Lambda\Phi\|_{B(l_1)}$ and $\|I - \Lambda\Phi\|_{B(l_\infty)}$, followed by estimation of $\|I - \Lambda\Phi\|_{B(l_2)}$ via Equation (16).

6.1 Estimation of $\|I - \Lambda\Phi\|_{B(l_1)}$

By looking at Equation (14), one realizes that what $\|I - \Lambda\Phi\|_{B(l_1)}$ does is column-wise summations. The terms $a_{\mu j} = |\varphi_\beta(\mu + j) / \varphi_\beta(\mu)|$ in Equation (14) are however rather hard to grasp. That is why we start by performing some simplifications on these. Let $h(t) = \cos \pi t / (t(1 - 4t^2))$, $t = \beta x$. Then

$$\begin{aligned} a_{\mu j} &= \left| \frac{\varphi_\beta(\mu + j)}{\varphi_\beta(\mu)} \right| = \left| \frac{\sin \pi(\mu + j)\pi}{\pi \sin \pi\mu} \frac{h(\beta(\mu + j))}{h(\beta\mu)} \right| \\ &= \left| \frac{(-1)^j \sin \pi\mu}{\sin \pi\mu} \frac{h(\beta(\mu + j))}{h(\beta\mu)} \right| = \left| \frac{h(\beta(\mu + j))}{h(\beta\mu)} \right|. \end{aligned}$$

Both $\varphi_\beta(x)$, $|\varphi_\beta(x)|$ and $a_{\mu j}$ are shown for different β in Figure 1.

Since $a_{\mu j} = a_{\mu(-j)}$ the estimates of the norm are done for $j \geq 1$ only.

Different values of the jitter error μ can be chosen for different integers j . To fulfill the supremum argument in Equation (14) we use the μ that maximizes each $a_{\mu j}$, for $j \in \mathbb{Z} \setminus \{0\}$, i.e., we derive

$$\sum_{j \neq 0} \sup_{|\mu| < \delta} \left| \frac{h(\beta(\mu + j))}{h(\beta\mu)} \right| \leq \frac{1}{|h(\beta\delta)|} \sum_{j \neq 0} \sup_{|\mu| < \delta} |h(\beta(\mu + j))|. \quad (25)$$

Note that we have the restriction $\beta\delta < 3/2$ since $|h(t)|$ decreases, hence $1/|h(t)|$ increases, only until the first zero of the function at $t = 3/2$. Since $\delta < 1/2$, β is restricted to $\beta < 3$ for this approximation. It is possible to confirm that $h(t) = (1/t) \cos \pi t / (1 - 4t^2)$ decreases on $t \in [0, 3/2]$ by analysis of the derivative of $g(t) = \cos \pi t / (1 - 4t^2)$ in the usual way and if $g(t)$ decreases so will $h(t)$ since $1/t$ decreases on the interval of interest.

Furthermore, we have used the fact that φ_β is a C^∞ function and looked for the supremum of $a_{\mu j}$ in the interval's endpoints and at possible singular and critical points. Neither of the singular points, all due to the absolute value, contribute to the supremum, since they are equal to zero. The critical points were found numerically by the bisection method and with an accuracy of order 10^{-6} for $h'(t) = 0$, which turns out to be equivalent to: $\tan \pi t = (12t^2 - 1) / (\pi t (1 - 4t^2))$.

Now, the sum in Equation (25) is an infinite sum, an impossible task for a computer program. To make the sum finite we introduce the integer m that guarantees that $\sum_{j=m}^{\infty} a_{\mu j} < \varepsilon$. Some straightforward calculations and Cauchy's integral test give the estimate of the sum

$$\begin{aligned} \frac{1}{|h(\beta\delta)|} \int_m^\infty \left| \frac{\cos \pi \beta x}{\beta x (1 - 4\beta^2 x^2)} \right| dx &\leq \frac{1}{h(\beta\delta)} \int_m^\infty \frac{1}{\beta x (4\beta^2 x^2 - 1)} dx \\ &= \frac{1}{h(\beta\delta)} \ln \left(1 + \frac{1}{4\beta^2 m^2 - 1} \right)^{1/2} < \varepsilon. \end{aligned}$$

Solving for m gives $m > ((1 / (e^{2h(\beta\delta)\varepsilon} - 1) + 1) / (4\beta^2))^{1/2}$. To be on the safe side, let

$$m = \left\lceil \frac{1}{2\beta} \left(\frac{1}{e^{2h(\beta\delta)\varepsilon} - 1} + 1 \right)^{1/2} \right\rceil,$$

where $\lceil x \rceil$ rounds $x \in \mathbb{R}$ towards nearest bigger integer. Altogether this gives

$$\|I - \Lambda\Phi\|_{B(l_1)} \leq 2 \sum_{j=1}^{m-1} \frac{1}{|h(\beta\delta)|} \sup_{|\mu| < \delta} |h(\beta(\mu + j))| + 2\varepsilon. \quad (26)$$

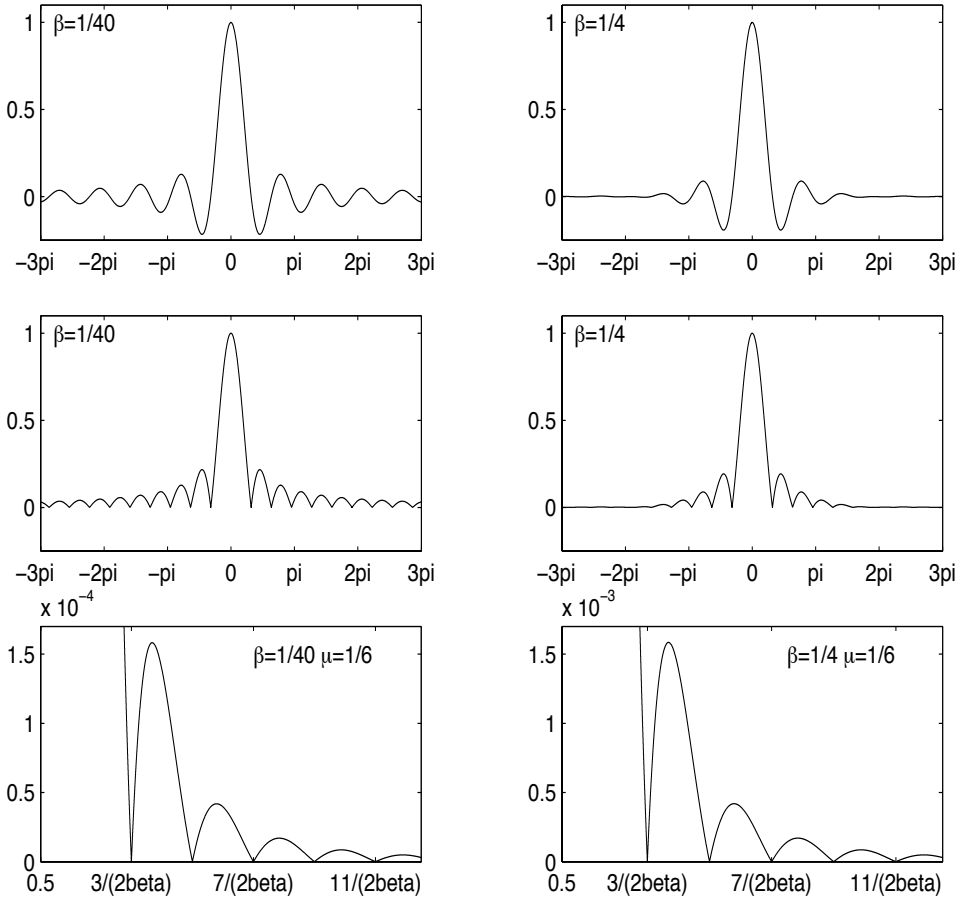


Figure 1: The sampling function $\varphi_\beta(x) = \frac{\sin \pi x \cos \pi \beta x}{\pi x (1 - 4(\beta x)^2)}$ on the top row, $|\varphi_\beta(t)|$ in the middle, and $a_{\mu j}$ on the bottom row.

6.2 Estimation of $\|I - \Lambda\Phi\|_{B(l_\infty)}$

The other norm, $\|I - \Lambda\Phi\|_{B(l_\infty)}$, is supremum of the absolute row sum. For each row, there is one μ , hence the question is which μ that gives the largest row sum. Due to symmetry, $|\varphi_\beta(\mu + j)| = |\varphi_\beta(-\mu - j)|$, hence

$$\begin{aligned} \|I - \Lambda\Phi\|_{B(l_\infty)} &= \sup_{|\mu| < \delta} \sum_{j \neq 0} \left| \frac{\varphi_\beta(\mu + j)}{\varphi_\beta(\mu)} \right| = \sup_{|\mu| < \delta} \sum_{j=1}^{\infty} (a_{(-\mu)j} + a_{\mu j}) \\ &\leq \sup_{|\mu| < \delta} \frac{1}{|h(\beta\mu)|} \sum_{j=1}^{\infty} (|h(\beta(j - \mu))| + |h(\beta(j + \mu))|) \\ &\leq \sup_{|\mu| < \delta} \frac{1}{|h(\beta\mu)|} \sum_{j=1}^m (|h(\beta(j - \mu))| + |h(\beta(j + \mu))|) + 2\varepsilon, \end{aligned}$$

where the same estimate of ε is used as in Section 6.1.

6.3 Experimental Results

Our goal was to estimate the upper limit of a possible error, caused by for instance an irregularity in the sampling process, that still makes it possible to retrieve the function from the sampled values. The theoretical aspects were presented in the previous sections and now it is time for the results from the computer aided calculations.

We have estimated $\|I - \Lambda\Phi\|_{B(l_1)}$ and $\|I - \Lambda\Phi\|_{B(l_\infty)}$ as suggested in Section 6.1 and 6.2 respectively, and used Equation (4) to get a satisfactory estimate of $\|I - \Lambda\Phi\|_{B(l_p)}$. For each β , the maximum δ that enables $\|I - \Lambda\Phi\|_{B(l_p)} < 1$ has been found with the bisection method with arbitrarily small error.

The results are shown in Figure 2, where δ is plotted for different β , $\beta \in (0, 3)$. As we can see the l_1 -norm is bigger, hence allows a smaller δ than the l_∞ -norm, and any other p gives a graph between the ones from the l_1 -norm and the l_∞ -norm. These results are expected from Equations (4), (14) and (15).

At first, as an immediate reaction, one might think that there is an error at the end of the l_1 -norm when the graph changes its tendency and suddenly decrease.s On top of that it seems to be decreasing as a straight line. This is however not the case. As β increases towards 3, the number of local maxima within every interval $[k - \delta, k + \delta]$ goes to 3, see Figure 1. Since the function decreases as $1/x^3$, the first local maxima are very important in comparison to the latter ones. This is enough to change the appearance of the graph. These theories are confirmed experimentally

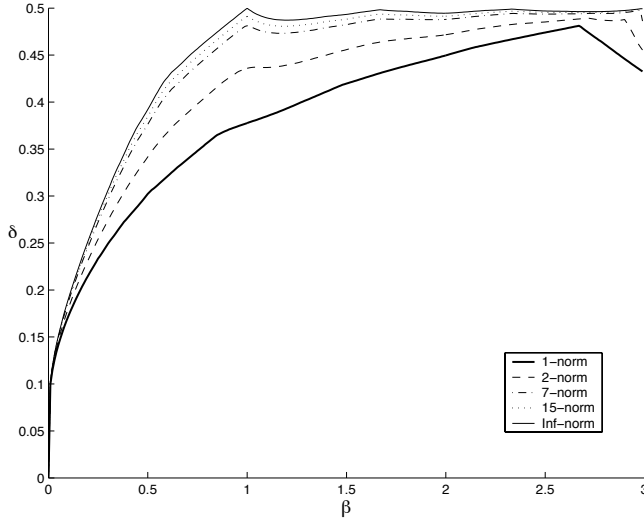


Figure 2: The simulated results, for a small number of norms, of the maximum irregularity δ with preserved possibility to retain the original function from the set of samples.

as follows. For $\beta \approx 3$ we have

$$\frac{1}{|h(\beta\delta)|} \sum_{j=1}^m \sup_{|\mu| < \delta} |h(\beta(\mu + j))| \approx \frac{1}{|h(\beta\delta)|} \sum_{j=1}^{m/3} |h(c_{3i-2})| = \frac{C}{|h(\beta\delta)|},$$

which can be compare to the estimate in Equation (26), where $h(c_{3i-2})$ gives every third local maxima. To check for which δ we have the restriction $C/|h(\beta\delta)| \leq 1$, we solve $\beta\delta = h^{-1}(C)$ and plot $\delta = h^{-1}(2C)/\beta$, see Figure 3.

6.4 Discussions and Further Work

In this section we give some suggestions for further work. At some points there are generalizations of the work done in this paper and at other points we suggest expansion to new areas.

We have worked with the sampling function $\varphi_\beta(x) = \text{sinc}(x)g(\beta x)$ in this paper, where $g(x) = \cos(\pi x)/(1 - 4x^2)$. Of course, we can use the same method on the more general sampling function $\text{sinc}(x)g(x)$, where g is required to fulfill some modest conditions. This gives various sampling functions φ , including the “standard” Shannon sampling function $\text{sinc}(x)$ for $g = 1$, and the Meyer scaling function which is very well known in the area of wavelet analysis. Moreover, it

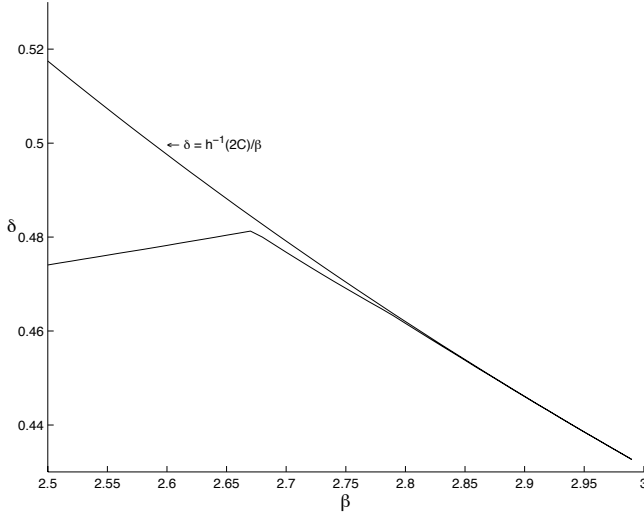


Figure 3: The lower graph in this figure is a magnification of the end of the 1-norm, see Figure 2. The upper graph confirms the theories that the decay is of the type $1/x$.

turns out that in some sense all examples of sampling functions that are suitable for sampling at the integers will be on the form $\text{sinc}(x)g(x)$ for some g . This will be dwelled upon in a forthcoming paper.

The use of $\text{sinc}(x)$ as sampling function within the method proposed in this paper leads to some technical difficulties. Both $\|I - \Lambda\Phi\|_{B(l_1)}$ and $\|I - \Lambda\Phi\|_{B(l_\infty)}$ in Equations (14) and (15) are infinite for this choice of φ since the rows and columns in matrix $I - \Lambda\Phi$ decay as $1/k$. However, for this particular case with the Shannon sampling function, the expansion

$$\begin{aligned} [\varphi(\lambda_k - j)] &= [\varphi(k - j + \delta_k)] \\ &= [\varphi(k - j)] + [\varphi(k - j + \delta_k) - \varphi(k - j)], \end{aligned}$$

may be made use of to come around the problem with slow decay. There are also some preliminary results that this might help for other examples of sampling functions too. Since the first part $[\varphi(k - j)]$ of the expansion is of “convolutional” type, Fourier methods induce representation by a multiplication after transformations. The other part, $[\varphi(k - j + \delta_k) - \varphi(k - j)]$, must be worked on with methods from this paper and it turns out that in many cases there will be faster decay, e.g. for Shannon the decays will be $1/k^2$.

Of course it is also of interest to explore how representation with the sampling function $\text{sinc}(x) \cos(\pi\beta x)/(1 - 4(x\beta)^2)$ in Section 6 works in a practical application when some kind of “real” data is sampled, processed and reconstructed. There is some work done in this direction, see e.g. [1] and [2] where an example with a MRI image is given.

In this paper we have considered the space $L_p(\mathbb{R})$. However, since general theory for irregular sampling in weighted shift-invariant spaces $L_{\nu,p}(\mathbb{R}^d)$ is developed, [2], we may also extend the problem and the entire theoretical framework suggested in this paper to higher dimensions.

References

- [1] A. Aldroubi. Non-uniform weighted average sampling and reconstruction in shift-invariant and wavelet spaces. *Applied and Computational Harmonic Analysis*, pages 151–161, 2002.
- [2] A. Aldroubi and K. Gröchenig. Nonuniform sampling and reconstruction in shift-invariant spaces. *Society for Industrial and Applied Mathematics*, pages 585–620, 2001.
- [3] J. Bergh, F. Ekstedt, and M. Lindberg. *Wavelets*. Studentlitteratur, 1999.
- [4] J. Bergh and J. Löfström. *Interpolation Spaces*, volume 223 of *Grundlehren der Mathematischen Wissenschaften*. Springer, Berlin, 1976.
- [5] C. S. Burrus, R. A. Gopinath, and H. Guo. *Introduction to Wavelets and Wavelet Transforms: A Primer*. Prentice Hall, Upper Saddle River, New Jersey 07458, 1998.
- [6] O. Christensen. *An Introduction to Frames and Riesz Bases*. Birkhäuser, 2002.
- [7] C. K. Chui. *Wavelets: A Mathematical Tool for Signal Analysis*. SIAM, 1997.
- [8] I. Daubechies. *Ten Lectures on Wavelets*. SIAM, Philadelphia, Pennsylvania, 1992.
- [9] P. Denbigh. *System Analysis & Signal Processing*. Addison Wesley Longman Ltd, 1998.
- [10] S. Ericsson and N. Grip. An analysis method for sampling in shift-invariant spaces. *International Journal of Wavelets, Multiresolution and Information Processing*. preprint.
- [11] N. Grip. *Wavelet and Gabor Frames and Bases: Approximation, Sampling and Applications*. PhD thesis, Department of Mathematics, Luleå University of Technology, 2002.
- [12] K. Gröchenig. *Foundations of Time-Frequency Analysis*. Applied and Numerical Harmonic Analysis. Birkhäuser, Boston, 2001.
- [13] E. Hernández and G. Weiss. *A First Course on Wavelets*. CRC Press, Florida, USA, 1996.

- [14] S. Mallat. *A Wavelet Tour of Signal Processing*. Academic Press, London, second edition, 1999.
- [15] Y. Meyer. *Wavelets and Operators*. Cambridge University Press, Cambridge, UK, 1992.
- [16] A. V. Oppenheim, A. S. Willsky, and S. H. Nawab. *Signals & Systems*. Prentice Hall Signal Processing Series. Prentice Hall, Upper Saddle River, New Jersey 07458, second edition, 1997.
- [17] L. Prasad and S. S. Iyengar. *Wavelet Analysis with Applications to Image Processing*. CRC Press LLC, 1997.
- [18] J. Schur. Bemerkungen zur Theorie der beschränkten Bilinearformen mit unendlich vielen Veränderlichen. *J. Reine Angew. Math.*, 140(1):1–28, 1911.
- [19] G. G. Walter. Non-uniform sampling in wavelet subspaces. *IEEE International Conference on Acoustics, Speech, and Signal Processing*, 4:2057–2059, 15–19 March 1999. ICASSP '99. Proceedings.
- [20] G. G. Walter and A. I. Zayed. Wavelets in closed forms. In L. Debnath, editor, *Wavelet Transforms and Time-Frequency Signal Analysis*, pages 121–143. Birkhäuser, Boston, 2001.
- [21] G. G. Walter and J. Zhang. Orthonormal wavelets with simple closed-form expressions. *IEEE Transactions of Signal Processing*, 46(8):2248–2251, August 1998.
- [22] P. Wojtaszczyk. *A Mathematical Introduction to Wavelets*. Cambridge University Press, 1997.
- [23] R. M. Young. *An Introduction to Nonharmonic Fourier Series*. Academic Press, 1980.

Towards automatic detection of local bearing defects in rotating machines

S. Ericsson, N. Grip, E. Johansson, L.E. Persson, R. Sjöberg, J.O. Strömberg, Towards automatic detection of local bearing defects in rotating machines, *Mechanical Systems and Signal Processing*, Vol. 19 (2004), 509-535.

Towards Automatic Detection of Local Bearing Defects in Rotating Machines

S. Ericsson,^{*} N. Grip,^{*} E. Johansson,^{*} L.E. Persson,^{*}
R. Sjöberg,[†] J.O. Strömberg[‡]

Abstract

In this paper we derive and compare several different vibration analysis techniques for automatic detection of local defects in bearings.

Based on a signal model and a discussion on to what extent a good bearing monitoring method should trust it, we present several analysis tools for bearing condition monitoring and conclude that wavelets are especially well suited for this task. Then we describe a large-scale evaluation of several different automatic bearing monitoring methods using 103 laboratory and industrial environment test signals for which the true condition of the bearing is known from visual inspection. We describe the four best performing methods in detail (two wavelet-based, and two based on envelope and periodization techniques). In our basic implementation, without using historical data or adapting the methods to (roughly) known machine or signal parameters, the four best methods had 9–13 % error rate and are all good candidates for further fine-tuning and optimization. Especially for the wavelet-based methods, there are several potentially performance improving additions, which we finally summarize into a guiding list of suggestion.

1 Introduction

Bearing failures in rotating machines can cause both personal damages and economical loss. Manual inspections are not only expensive, but also connected with a risk of accidentally *causing* damages when reassembling a machine. Thus there is a clear need for non-destructive methods for predicting bearing damages early enough to wait with bearing replacements until next scheduled stop for machine

^{*}Department of Mathematics, Luleå University of Technology, SE-97187 Luleå, Sweden

[†]Nåiden Teknik AB, Aurorum 30, SE-977 75 Luleå, Sweden

[‡]Department of Mathematics, Royal Institute of Technology, SE-100 44 Stockholm, Sweden

maintenance. The most successful such methods in use today are all based on vibration analysis (see, e.g., [34, 35]). They do, however, require special competence from the user, whereas, as the industry optimizes there is less personnel and time available for condition monitoring. Thus important information to support decisions is lost and there is a demand for more automatized and supportive bearing monitoring software.

Classical bearing monitoring methods can usually be classified as either time domain methods (see, for example, [3, 4, 8, 20]) or frequency domain methods (see, for example, [22, 28, 31, 33]). These methods look for periodically occurring high-frequency transients, which however is complicated by the fact that this periodicity may be suppressed. Moreover, classical Fourier methods tend to average out transient vibrations (such as those typical for defect bearings), thus making them more prone to “drown” in the background noise of harmless vibrations. A natural countermove is to use methods that show how the frequency contents of the signal changes with time. This kind of analysis is usually referred to as time-frequency analysis. The *continuous wavelet transform* (CWT) is one such transform which is particularly good at separating the short high-frequency outbursts of a typical localized bearing defect from long-duration low-frequency signal components (occurring, for example, at multiples of the axis rotational frequency). Since its introduction in the mid-eighties the theory of wavelets has grown very rapidly in almost every field of signal processing and recently research has begun in areas of mechanical vibration analysis (see, for example, [5, 6, 16, 17, 26, 29, 32, 36]).

However, it is extremely important to point out that a new analysis technique only can provide more reliable diagnoses if the new mathematics and signal processing are combined with a deep insight into and experience of different types of rotating machinery.

This was the starting point of a unique Swedish joint research project with participation from Nåiden Teknik, the Centre of Applied Mathematics (CTM) at Luleå University of Technology, the Royal Institute of Technology (KTH) in Stockholm, the Swedish Institute of Applied Mathematics (ITM), and the three forestry combines AssiDomän, Modo and StoraEnso. This text is a condensed and rewritten version of selected parts of the final report [9] of that project.

The final goal is an automatic bearing monitoring system with easily interpreted output data that reflects the probability of a defect bearing (see Figure 1).

We divide this analysis into three steps: First some analysis method is applied to an acceleration measurement \mathbf{a} (here usually of length $N = 16\,384$). The analyzed signal \mathbf{b} requires some expert knowledge for a correct interpretation. Depending on the analysis method, the length N' of \mathbf{b} is usually comparable to N (or even N^2 for 2D-plots). This is too much for standard classification methods. Thus, as an intermediate step, we need to pick out the important information from

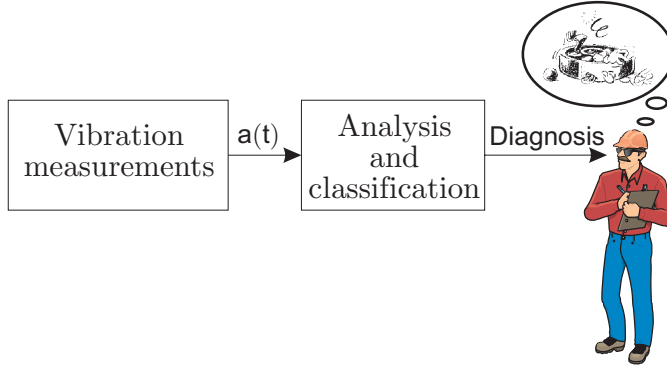


Figure 1: The final goal is an automatic and user-friendly bearing condition monitoring system.

\mathbf{b} and reduce it to some n -dimensional \mathbf{c} for a reasonably small n (e.g., $n = 2$ in plots like the one in Figure 10) (b)). Then a classification method can give the desired automatic diagnosis “functional” or “defect” (possibly with some additional judgment about the type and size of the defect):

$$\mathbf{a} \in \mathbb{R}^N \xrightarrow{\text{Analysis}} \mathbf{b} \in \mathbb{R}^{N'} \xrightarrow{\text{Reduce dimensionality}} \mathbf{c} \in \mathbb{R}^n \xrightarrow{\text{Classification}} \text{Diagnosis}$$

With the additional diagnostic power of such a method, maintenance staff will have a powerful tool and more time and concentration left for other important tasks.

In Section 2, we discuss important characteristics of and differences between different condition monitoring methods. The main focus is on the importance of a signal model and to what extent it should be trusted. Section 3 is a more detailed overview of different mathematical tools that can be combined into an immense number of different bearing monitoring methods. From these, we have chosen reasonable combinations, implemented them in MATLAB and compared using a large number of test signals (see Section 4) from both laboratory and industrial environments. Finally, we present our most promising results so far in Section 5.

All symbols and notation will be explained when it first appears in the text. The most frequently used notation is also collected in Table 2.1.

2 The signal model and its importance

The methods that we have considered range from methods that rely heavily on a detailed signal model to methods that work more “blindly” but without the risk of assuming too much. The former methods may perform better, but only if the model

is “good enough”. If the differences between model and reality are “too big” or fluctuate “too much”, then a more robust method is required. We have grouped the evaluated methods into the following three categories (see also Figure 2):

- *Matched filters* and *Cramér-Rao estimation* are examples of methods that rely hard on a rather detailed signal model.
- The largest block of methods are well established time- and frequency domain methods, as well as techniques based on time-frequency analysis. They depend less on the signal model and should therefore in general be more robust. The evaluation of these methods is complicated by the fact that there are so many tools to play with. It is not possible to evaluate all possible (combinations of) methods and all more or less important choices associated with each method, such as the choice of wavelet, thresholds, what frequencies to investigate etc. Therefore, one must restrict to comparing a reasonably small number of methods that seem likely to perform well.
- Similar to the first two mentioned methods, *feature extraction* is in a certain sense an optimal way to detect bearing faults, but now in the case when no reliable signal model is available. Instead, these methods are trained on test signals of all types that the methods shall be able to tell apart. Thus many test signals are needed and they cannot be created artificially (since that would require a reliable signal model and if one exists, it is our strong belief that one can achieve better performance with a bearing monitoring method based

Notation	Meaning
$a(t), s(t)$ etc, $t \in \mathbb{R}$	Continuous time signals.
$a[k], s[k]$ etc, $k \in \mathbb{Z}$	Sample values ($a[k] = a(kT)$ etc.).
$\mathbf{a}, \mathbf{b}, \mathbf{c}$ etc.	Vectors.
$a(t)$	Measured acceleration of vibrations $s(t)$.
a_d	Decay parameter of impulse response h .
f	Frequency variable.
f_0	Bearing-axis resonance frequency.
$h(t)$	Impulse response of the bearing-axis system.
$s(t)$	Bearing vibrations ($s''(t) = a(t)$).
t	Time variable.
A	Amplitude of impact oscillations.
CWT	Continuous Wavelet Transform.
FFT	Fast Fourier Transform.
$S(f), H(f)$ etc.	Fourier transforms: $S(f) \stackrel{\text{def}}{=} \int_{\mathbb{R}} s(t) \exp^{i2\pi f t} dt$

Table 2.1: Notation used throughout the paper. All temporarily used symbols and notation are defined as they appear in the text.

on this model).

Exact knowledge of the impulse response $h(t)$ would decrease the complexity and improve the performance of several methods presented in this report. Although we have special (and not too expensive) measure equipment for measuring h , this equipment does require some special competence from the user. Thus it is unrealistic to assume h to be exactly known in a typical industrial environment, where these measurements has to be done at some 2000 different measure points. We are therefore limited to *theoretical* models.

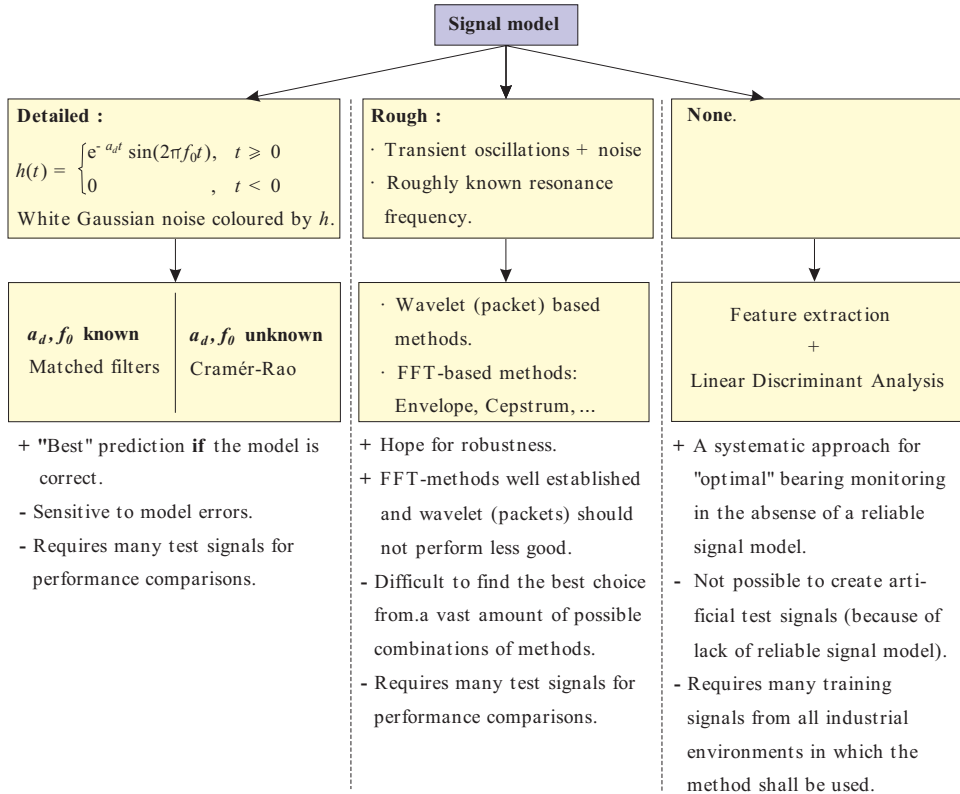


Figure 2: Overview and classification of bearing monitoring methods. A more detailed model of bearing fault vibrations $h(t)$ and noise improve theoretical performance at the cost of larger sensitivity to model errors.

2.1 A rudimentary signal model

We will now propose a rudimentary mathematical model for what we mean is the most important vibration measurement characteristics that a good bearing monitoring method must recognize.

An impact impulse is generated every time a ball (or roller) hits a defect in the raceway or every time a defect in a ball hits the raceway. Each such impulse excites a short transient vibration in the bearings at its natural frequencies. The lowest such frequency, f_0 , is a rigid body mode (individual balls acts as springs, see [13, page 996]). We will often refer to f_0 as the *resonance frequency* of the bearing.

As in [13, Chapter 26], we model the shaft-bearing system as a viscously damped mass-spring system, but instead of applying an oscillating force, we are interested in the vibrational response of the bearing and its surroundings to the impact impulses. Each impact causes an instantaneous increase of the momentum, which can be used as initial condition for the position $h(t)$ of the point where vibration measurements are performed. A standard solution (see, for example, [23]) gives the impulse response

$$Ch(t) \stackrel{\text{def}}{=} \begin{cases} Ce^{-a_d t} \sin(2\pi f_0 t) & \text{if } t > 0, \\ 0 & \text{otherwise,} \end{cases} \quad (1)$$

where a_d is a decay (or bandwidth) parameter.

As the shaft rotates, these vibrations will occur periodically with an *impact frequency* $1/T$ (computed in (2.1) below). With notation A_p for the impact impulse amplitudes and $A \stackrel{\text{def}}{=} A_p C$, the resulting signal is

$$s(t) = A \sum_n h(t - nT). \quad (2)$$

Since s is the convolution of Ah with a T -periodic sequence of Dirac delta-distributions, $p_T \stackrel{\text{def}}{=} \sum_n \delta(\cdot - nT)$, its Fourier transform is

$$S(f) = AH(f)P_T(f) = \frac{A}{T}H(f) \sum_n \delta\left(f - \frac{n}{T}\right).$$

Both s and \hat{s} are sketched in Figure 3 (where the Dirac impulses are denoted with vertical arrows, showing up as well-localized sharp impulses in real applications). There, the largest peaks appear around frequency f_0 , but in real measurements this frequency localization can be displaced towards lower frequencies as the bearing defect grows bigger. This would not happen if only the impact amplitude A_p was

growing. Instead we interpret this as a sign that for large defects, p_T is sometimes better modeled as a train of rectangles

$$p_T(t) = A_p \sum_{n=-\infty}^{\infty} r_{\varepsilon}(t - nT), \quad r_{\varepsilon}(t) = \begin{cases} \frac{1}{2\varepsilon} & \text{if } |t| < \varepsilon \text{ for some integer } n, \\ 0 & \text{otherwise.} \end{cases}$$

Hence, with $*$ denoting convolution, this change of p_T will replace the vibrations s with $s_{\varepsilon} \stackrel{\text{def}}{=} Ap_T * h$ such that

$$\begin{aligned} s_{\varepsilon}(t) &= A \sum_{n=-\infty}^{\infty} \int_{-\infty}^{\infty} r_{\varepsilon}(t - \tau - nT) h(\tau) d\tau \\ &= A \sum_{n=-\infty}^{\infty} \int_{-\infty}^{\infty} r_{\varepsilon}(-\tau) h(t - nT + \tau) d\tau \\ &= \frac{A}{2\varepsilon} \int_{-\varepsilon}^{\varepsilon} \sum_{n=-\infty}^{\infty} h(t - nT + \tau) d\tau = \frac{1}{2\varepsilon} \int_{-\varepsilon}^{\varepsilon} s(t + \tau) d\tau. \end{aligned}$$

Hence, s is a smeared out local average $s_{\varepsilon} = s * r_{\varepsilon}$ of s with Fourier transform

$$S_{\varepsilon}(f) = S(f)R_{\varepsilon}(f) = S(f) \frac{\sin(2\pi f\varepsilon)}{2\pi f\varepsilon},$$

where $\left| \frac{\sin(2\pi f\varepsilon)}{2\pi f\varepsilon} \right|$ decays as $1/|f|$ when $|f| \rightarrow \infty$. This means, roughly, that the dominating parts of S are displaced from f_0 towards lower frequencies.

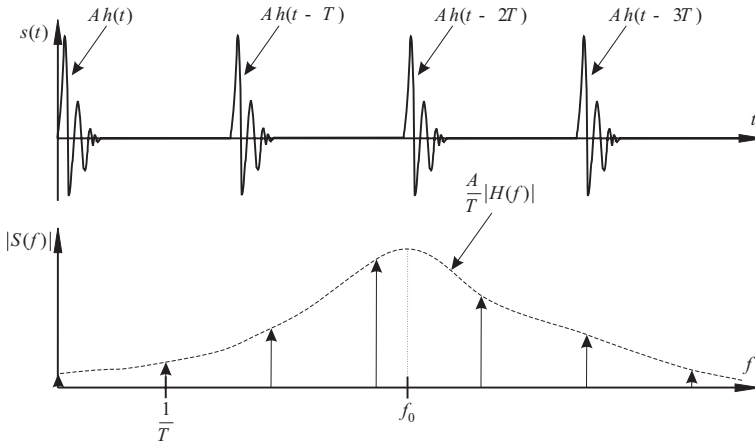


Figure 3: Sketch of vibrations caused by a typical localized bearing defect.

Equations (1) and (2) suggest that a good bearing monitoring method should be designed to look for transient oscillations of frequency f_0 and check whether these oscillations occur periodically with a period T (note however, that it should not depend too heavily on this periodicity, as explained in Section 3). The location of a defect can then be identified if $1/T$ coincides with one of the following frequencies, which are computed from the geometry of the bearing (see [13, Chapter 8] for details):

$$\text{Cage frequency: } f_C = \frac{f_A}{2} \left[1 - \frac{D_b}{D_p} \cos(\varphi) \right]. \quad (3a)$$

$$\text{Outer race frequency: } f_O = \frac{1}{T_O} = N_b \cdot f_C. \quad (3b)$$

$$\text{Inner race frequency: } f_I = \frac{1}{T_I} = N_b(f_A - f_C). \quad (3c)$$

$$\text{Roller (or ball) spin frequency: } f_R = \frac{1}{T_R} = \frac{D_p}{2D_b} f_A \left[1 - \left(\frac{D_b}{D_p} \right)^2 \cos^2(\varphi) \right]. \quad (3d)$$

Here we used the following notation:

- f_A = revolutions per second of inner race,
- D_b = ball diameter,
- N_b = number of balls,
- D_p = pitch circle diameter and
- φ = contact angle.

These formulas are theoretical and the difference between calculated and measured bearing frequencies can be as much as several Hertz. These discrepancies arise when bearings have significant thrust loads and internal preloads. This changes the contact angle and causes the outer race frequency to be higher than calculated (see [35, page 150]).

2.2 Loaded bearings

Only the model (2) for s , is used in simulations and methods described in the remaining paper. For loaded bearings with inner race or rolling element faults, the following refinements can be useful.

For a loaded bearing, the impact impulses can be written

$$p(t) = \sum_{l=-\infty}^{\infty} A_p \beta(\tau + lT) \delta(t - \tau - lT) \quad (4)$$

with nonzero amplitude A_p if a defect bearing is present. The delay τ depends on where on the ball or raceway the defect is located. For an outer ring fault, $\beta(t) = 1$. For an inner race fault, β describes how the strength of the impulses varies when the defect moves into and out from the load zone. For radial load, Harris [13, pages 234–236] suggests the model¹

$$\beta(t) = \max \left(1 - \frac{\varepsilon}{2} (1 - \cos(2\pi f_A t - b)), 0 \right)^\alpha, \quad (5a)$$

where $\varepsilon > 2$ for a bearing with positive clearance and α is $3/2$ for ball bearings and $10/9$ for roller bearings. (This model can more or less be found in [3, 22].) A bigger exponent α gives a more pointed envelope β . The plot in Figure 4(a) illustrates how ε and b affect the shape and translation of β .

In this survey, we will only consider inner and outer ring defects. For detection of rolling element faults we suggest to add a factor $(-1)^l$, which reflects the fact that every second rolling element impact hits the inner ring and every second impact hits the outer ring (see Figure 4(b)), that is, to replace $\beta(t)$ in (4) with

$$\beta_l(t) \stackrel{\text{def}}{=} (-1)^l \max \left(1 - \frac{\varepsilon}{2} (1 - \cos(2\pi f_C t - b)), 0 \right)^\alpha. \quad (5b)$$

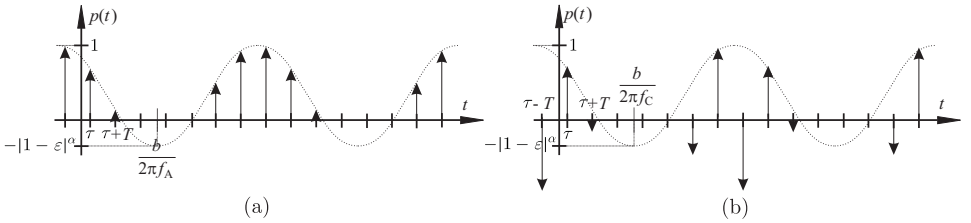


Figure 4: Example plot of the impact impulses $p(t)$ in the case of an inner ring fault (a) and an rolling element fault (b). Each Dirac impulse $A_p \beta(\tau + lT) \delta(t - \tau - lT)$ in (4) is drawn as a vertical arrow with length equal to the impulse amplitude. The positive part of the dotted “envelopes” are the functions β and β_l in (2.2).

2.3 Adding noise and discretising

It remains to adapt our model for *continuous-time position-measurements* (2) to the actual *bandpass filtered* and *noisy acceleration-measurements* treated in the

¹Our ε correspond to $1/\varepsilon$ in [13], because then the case of no load simply corresponds to setting $\varepsilon = 0$ in computer simulations.

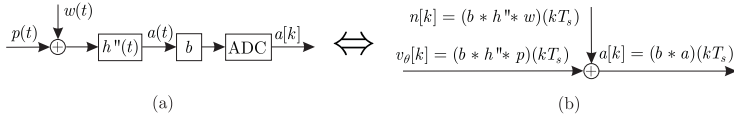


Figure 5: The continuous time (a) and equivalent discrete time (b) system models. The sampling is performed by a bandpass filter b and an analog-to-digital converter (ADC).

remaining paper. We base this model on the underlying assumption that all other vibrations that the shaft-bearing system is exposed to add up to zero-mean white Gaussian noise w . This is in no way obvious but seems reasonable and a basic comparison of model and reality in Section 2.4 gives some support for this assumption. With $*$ denoting convolution, (4) gives the resulting measured acceleration

$$a(t) = \frac{d^2}{dt^2} ((p + w) * h)(t) = \sum_{l=-\infty}^{\infty} A\beta(\tau + lT)h''(t - \tau - lT) + (w * h'')(t). \quad (6)$$

Thus, we get the model depicted in Figure 5(a) and, after lowpass filtering and sampling, the equivalent discrete-time model in Figure 5(b) (for more details, see [9, Appendix C] and [24]).

2.4 Model verification and suggested refinements

Contrary to our assumption in Section 2.3, suppose that the sum of vibrations from different parts of a “typical” machine adds up to white Gaussian noise *after* the convolution with h'' . This would remove what we think of as the main complication of bearing condition monitoring (see Section 3.4), namely that and both the signal and the noise are “coloured” by the same filter h'' .

In Figures 6 and 7 we compare our signal and noise model with real measurements. For a simple but illuminating visual comparison, we plot the absolute value of the continuous wavelet transform (CWT) of the compared signals (as described in Section 3.3). Figure 6 shows a clear difference (in smoothness and frequency localization) between bandpass filtered white Gaussian noise (the lowermost plot) and the test rig vibration measurements from a functional bearing in the topmost plot. This plot looks more like the topmost plot in Figure 7, which shows Gaussian noise colored according to our model. The other plots in that figure show how increasing signal-to-noise ratio (SNR) gradually transforms the CWT to one more similar to the CWT of vibrations caused by a big outer race defect shown in the middle plot of Figure 6. Still, there are some differences in the exact shapes of the

bumps and fast Fourier transform (FFT) plots of some test signals also show deviations from our model at low and high frequencies. Thus, methods that rely much on a precise signal model may require further model refinements for good performance. Based on the above observations, we give a few suggestions for improving model correctness:

- To use a more detailed model of h and/or to adjust bandpass filters to (if possible) include possible resonance frequencies but block frequency bands where model deviations are known or believed to exist.
- Additional white or colored noise at low frequencies. Perhaps colored by

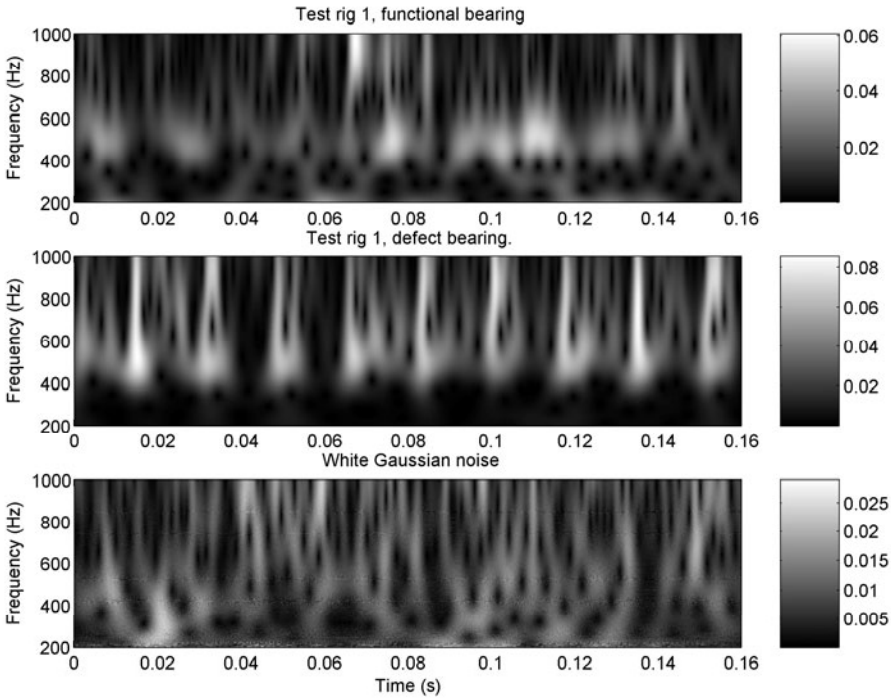


Figure 6: The topmost two plots show continuous wavelet transforms (CWT) of test rig measurements. The clear difference from the lowermost CWT of white Gaussian noise (bandpass filtered as described in Section 4.1) confirms that the noise is not white and Gaussian. Instead, the topmost two plots show more resemblance with corresponding plots in Figure 7, which is computed from our signal and noise model.

other parts of the measurement environment (e.g., there is often disturbing vibrations like vibrations oscillating with multiples of the axis rotational frequency or twice the motor feeding frequency).

- Other natural frequencies of the bearing-axis system [13, page 996] may be dominating the signal at higher frequencies.

3 Choice of basic methods

Underlying our choice of bearing monitoring methods to evaluate, are the following observation and restrictions:

- As described in Section 2.2 (and observed in some of our test signals), the load zone dependence of inner race bearing defects can suppress the period-

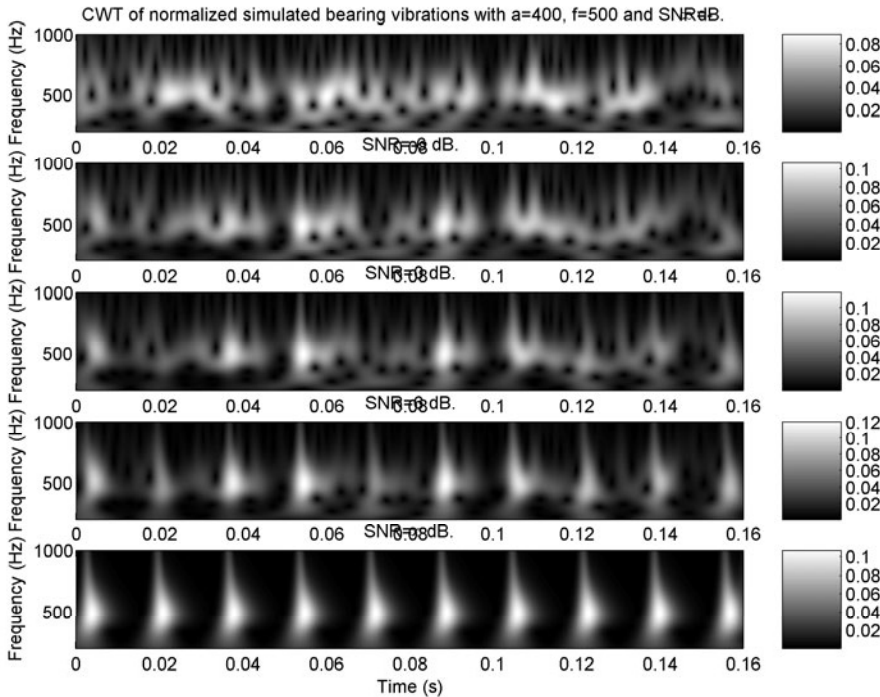


Figure 7: CWTs of simulated bandpass filtered bearing impacts with different signal-to-noise ratios.

icity of the bearing impacts. This makes such defects more difficult to find with a method that depends on this periodicity (such as the Fourier methods in Section 3.2) whereas the performance of methods that only reacts on a single (large enough) impact would be left unaffected. Still, this is no motivation for ignoring the extra information contained in the (possibly suppressed) impact periodicity.

On the contrary, in Section 3.4 we will see from matched filter theory that it is possible to obtain maximum signal-to-noise ratio for the bearing impacts by convoluting with the “inverse” of the impulse response h and look for the original impact impulses in white Gaussian noise, which by nature already contains large but rare impulses. Thus a single impact can be interpreted as a probable bearing defect only if it has *very* large amplitude (relative to the standard deviation of the noise), so that it is *very* unlikely that it is just a natural part of the white noise. For impulses that repeat with a (possibly suppressed) frequency coinciding with the inner ring impact frequency, much smaller impulse amplitudes are needed for detecting an equally probable inner ring defect. This is also the reason why, in Figure 6, some minor “bumps” are visible at the resonance frequency also in the first plot. The important difference is that in the second plot one can conclude from the amplitude and periodicity of the bumps that they originate from a large outer ring defect. *Thus it is our strong opinion that although it is desirable for a bearing monitor method to be able to detect a single (and large enough) impact, an optimal (in any reasonable sense) method must also be able to detect impact periodicity (suppressed or not) of possibly smaller impacts.*

- Another important matter is whether old measurements are available or not. In this text we aim for reasonably good performance *without comparing with old measurements*. Then the performance of all considered methods will surely improve with time, when there are old measurements to compare with.
- Similarly, although the actual vibration amplitude can be significantly different depending on the kind of bearing and environment, the amplitude *does* bring important information if it can be compared to the amplitude of some well-known signal component or some computed threshold reference value, but the following methods *analyze only the shape* of the signal (most methods will be homogeneous and this even includes nonlinear thresholding for certain threshold functions). So to assure a fair comparison of methods, all test signals are normalized to L_2 -norm $\|s\|_2 = \sqrt{\sum_n |s_n|^2} = 1$. Once again, in situations where we have something to compare with, the original norm can be used to improve the performance of all tested methods.

Based on these restrictions, we have chosen to evaluate methods that are based on the following basic tools (described in more detail in the original report [9]). The evaluation results for the so far best performing such methods then follow in Section 5.

3.1 Time methods

Kurtosis and crest factor: Some common “peakiness” estimates of a signal s are the *Kurtosis factor* $\|s - \bar{s}\|_4^4 / \|s - \bar{s}\|_2^2$ (where \bar{s} denotes the mean of s and $\|x\|_n^n \stackrel{\text{def}}{=} \sum_k |x_k|^n$), the *crest factor* $\max_k |s_k| / \|s\|_2$ (see, e.g., [3, 8]) and other variations on the same the same theme.

Autocorrelation and cepstrum: The *autocorrelation* of $s[k]$ is defined by

$$a_s[n] \stackrel{\text{def}}{=} \frac{1}{2N+1} \sum_{n=-N}^N s[k]s[k-n]^*$$

with $*$ denoting complex conjugate. With uppercase notation for the *discrete Fourier transform* $S[k] = \frac{1}{\sqrt{2N+1}} \sum_{n=-N}^N s[n] \exp^{-i\frac{2\pi k}{2N+1}n}$ it follows from the Parseval relation and the $2N+1$ -periodicity of $S[k]$ that

$$a_s[n] = \frac{1}{2N+1} \sum_{k=-N}^N s[k]s[k-n]^* = \frac{1}{2N+1} \sum_{k=-N}^N |S[k]|^2 \exp^{i\frac{2\pi k}{2N+1}n},$$

$$A_s[k] = \frac{1}{\sqrt{2N+1}} |S[k]|^2, \quad k = -N, -N+1, \dots, N,$$

where, under standard assumptions about ergodicity and “large enough” N , $|S[k]|^2 / (2N+1)$ is the *power spectrum* of s (see, e.g., [24, 25]). A related mathematical tool is the *cepstrum* c_s defined via its discrete Fourier transform

$$C_s[k] = \log |S[k]|^2, \quad k = -N, -N+1, \dots, N$$

and described in more detail by Randall [27]. He argues that the power spectrum of a faulty ball bearing may contain small scale (compared to the largest peaks in the spectrum) periodic structures that can appear clearly in c_s but not in a_s . Periodicities in s , with period T , will show as peaks in a_s and c_s at integer multiples of T .

Periodization: Another tool for making $1/T$ -periodic impacts more visible is the transformation

$$s \mapsto p(s) \stackrel{\text{def}}{=} \frac{1}{N \max |s|} \sum_{n=0}^{N-1} s(\cdot + nT) \Big|_{[0,T)}. \quad (7)$$

The function p emphasizes parts of s that are periodic with repetition frequency $1/T$. Since the outbursts we are searching for have rather high oscillation frequency, the estimated value of $1/T$ has to be quite accurate. Note, for a simple example, that $\cos(10^{17}x) + \cos(10^{17}(x + T))$ is very sensitive to small changes in T , whereas a demodulation of the cosines completely removes this sensitivity. Hence, we suggest to first demodulate s . In our implementations, we have in fact computed $p(d(b(s)))$, where b is a band-pass filter that cuts out the interesting frequency range (150–1000 Hz) and the *demodulation* d computes the absolute value of the analytic version of s . The analytic version of s (also called the *Hilbert transform* of s) is defined as twice the inverse Fourier transform of $u(f)S(f)$, where u is the unit step function.

Note 1 *Our periodization function p is related to synchronous time averaging (see, e.g., [35]), which uses a trigger, placed, e.g., on the axis for an exact synchronization of the data collection with the rotational speed of the axis. Usually the average of at the very least 100 measurements are computed, and the method is used to "average out" frequencies that not are multiples of the rotational frequency. Synchronous averaging can therefore be useful, e.g., for finding defects in gears. For the handheld devices and industrial applications that we have in mind, at most 20 averages is possible and triggers are too time-consuming and therefore "replaced" by deconvolution.*

3.2 Frequency methods

Power spectrum: The classical use of the Fourier transform is to search for the periodically repeated peaks in the power spectrum shown in Figure 3 (also described, e.g., in [27, 34, 35]).

Envelope method: The resonance frequency oscillation of the impacts and the possibly suppressed impact periodicity are two modulations of the vibrations that both reduce the amplitude of the power spectrum peaks, which therefore are more likely to be suppressed below the overall noise level. A popular

countermove is to remove the resonance frequency modulation with the *envelope method*, which consists of a bandpass filter (including the resonance frequency) followed by a demodulation and a fast Fourier transformation (see Figure 8 and for complementary details, e.g., [27]).

Both these methods use a bandpass filter to focus on a range of frequencies which must be wide enough to include the (roughly known) resonance frequency. Thus it is likely that also oscillation frequencies where bearing impact oscillations not are dominating are included in the analysis, with consequences such as lower signal-to-noise ratio and more sensitivity to possible suppressions of the impact periodicity.

3.3 Time-frequency methods

Time-frequency analysis provides tools for a more systematic bandpass filtering at a whole range of possible oscillation frequencies with “optimally sharp” bandpass filters (the Morlet wavelet below). This makes it possible to combine the good properties of frequency methods with an automatic search for exactly the oscillation frequencies (if any) where periodically repeated transients can be most clearly detected. Due to the resulting higher signal-to-noise ratio, we also expect such methods to be less sensitive to suppressions of the impact periodicity.

Continuous wavelet transform (CWT): We have chosen to use the CWT for time-frequency analysis, because it is good at separating transient high-frequency outbursts (such as bearing impacts) from the long-duration low-frequency vibrations typically appearing around, for example, the axis rotational frequency. For optimal simultaneous time- and frequency resolution (in the sense of minimal Heisenberg box area), we use a Morlet wavelet. For more about both this and a brief introduction to time-frequency analysis in general, see, e.g., [7, Chapter 1] or [11, Chapter 1].

In plots of the CWT amplitude, (such as Figure 6), “large enough” bearing impact vibrations appear as periodically occurring “bumps”, visible for the human eye. As described in the beginning of this section, due to the coloured

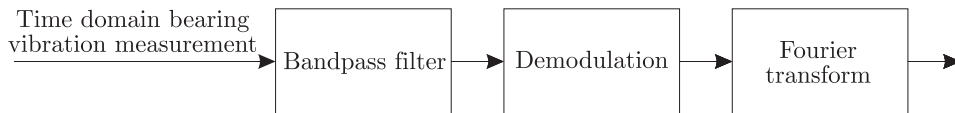


Figure 8: A block scheme for the *envelope method*. In our implementations, we have used the absolute value of the Hilbert transform for demodulation.

noise, the difference between *smaller* defects and functional bearings is more difficult to see from visual inspection of a CWT plot, so a more systematic analysis is required for telling these cases apart. We propose and evaluate two such methods in Section 5.3.

The CWT and wavelet packets (discussed below) are the computationally most expensive tools discussed here, but since the analysis is to be done on a separate personal computer and not by the measuring device, this complexity is not a problem.

Discrete wavelet transform (DWT): For a certain class of wavelets, all information about the original signal is contained in only a discrete set of points of the CWT. These point values can be computed very fast with the DWT. It lacks the optimal simultaneous time- and frequency resolution of the Morlet CWT and is not intended for visual inspection, but is a very powerful tool for, for example, noise reduction. One way to do this is to modify the wavelet coefficients using (hard or soft) threshold functions (see, e.g., [2, 21] for more details) and then compute the inverse DWT. There is much work behind the “correct” choice of threshold function. Several algorithms are proposed in the literature. However, most of them assume Gaussian white noise. Noise reduction is also a natural first step in virtually any other analysis method.

Wavelet packets: The wavelet packet transform is a generalization of the DWT that, in combination with a suitable chosen cost function for the best basis algorithm (see, e.g., [21] for details) also can be very useful for bearing condition monitoring. However, it requires a lot of work to find a suitable cost function that enhances bearing faults.

Gabor and Wigner-Ville transforms: These transforms can be used as the continuous wavelet transform and at least the Gabor transform has a relatively fast discrete version. (See, e.g., [12, 21].)

3.4 Statistical methods

Matched filters: With notation as in Figure 5 but without the bandpass filter b , we can easily compute the actual vibrations s from their measured second derivative a (by integration or, as a simple approximation in practical applications, with cumulative sums). Hence if h has strictly nonzero Fourier transform H , then there exists a filter m , $M(f) = 1/H(f)$, such that the original impacts and white Gaussian noise can be reconstructed with the convolution $p + w = m * s$. In fact, for our model, with h given in (1), all

this is possible and a straightforward computation gives a simple formula for m :

$$m(t) = \frac{1}{2\pi f_0} \left((a_d^2 + 4\pi^2 f_0^2) \delta(t) + 2a_d \delta'(t) + \delta''(t) \right), \quad (8)$$

where δ is the Dirac delta distribution. It follows from matched filter theory (see, e.g., [25]), that the filter m is optimal in the sense that it maximizes the signal-to-noise ratio (SNR). Hence, for maximal SNR, (8) shows that one should analyze the signal

$$p(t) + w(t) = s * m(t) = \frac{(a_d^2 + 4\pi^2 f_0^2)s(t) + 2a_d s'(t) + s''(t)}{2\pi f_0}. \quad (9)$$

Since s , s' and s'' are quite similar in shape and oscillation frequency, we expect that a *very precise model and parameter knowledge is required* for the terms in (9) to really add up to the original impact impulses and (in a noise-free environment) vanish elsewhere.

For the actual bandpass filtered input of a practical application, a more precise computation would replace (9) with a discrete-time convolution with the Fourier series coefficients of the corresponding bandpass filtered $m(t)$.

Recall also that, a_d and f_0 have to be guessed. Thus in a practical situation we can only hope for (the bandpass filtered version of) (9) to give nearly optimal SNR.

Since the parameters in (9) are roughly known for our test rig signals, we have applied (9) to measurements on a bearing with a *very* large defect (audible when the test rig is running) for a reasonably large number of possible parameter values. Still, this was not enough to result in an SNR-improvement visible for the eye. This simple test indicates a need for either a more precise signal model or a more robust analysis method, so the existence of a matched filter seems to be mainly of theoretical importance (as in the beginning of Section 3). A more detailed study would be interesting but is out of the scope of this paper.

Cramér-Rao lower bound: A minimum variance unbiased estimator \hat{A} of the bearing defect amplitude A (with amplitude $A = 0$ meaning “no defect”) is the estimation theory name for an analysis method which, given a vibration measurement, computes an estimate \hat{A} of A , and which on average will find the correct value (that is, it is *unbiased*). Moreover, it is an optimal such method in the sense that the average squared error (the *variance*) is minimal. In our case we have a few more unknown parameters (such as

a_d and f_0 in (1)), that can be grouped into a vector θ . There is an lower bound (the *Cramér-Rao lower bound*) for the error covariance of any linear method for estimating θ and a standard way for computing it, which however turned out not to be practically useful due to numerical problems in a test-implementation for our model and signals. All this and some alternative computational approaches is described in full detail in [9, Appendix D.2].

3.5 Feature extraction

A sampled version of the continuous wavelet transform with 128 scales containing 16 384 samples each can be seen as one point in $\mathbb{C}^{2^{21}}$. The name *feature extraction* is used for a collection of methods for reducing the number of dimensions by mapping this point to an element in, say, \mathbb{C}^{10} , but without removing “too much” relevant information. Relevant here means that it still is possible to separate functional bearings from faulty ones. Feature extraction is usually combined with a *classification* method (corresponding to the classification lines in the plots of Section 5).

In [14] and [9, Appendix B] we describe in detail an implementation of a wavelet-based feature extractor called *local discriminate bases* (LDB). The first results were promising but a more full-scale evaluation would require both a large set of training data and then a large-scale test on another large set of test signals. This is out of the scope of this article.

4 Experimental setup

From a larger set of measurements, we have chosen 81 industrial and 22 laboratory signals for which the size of all bearing faults are known from manual inspections. For easy reference, we will use the same names on plotted signals as in [9, p. 58–64], which is a detailed descriptions of the signals, bearings machines and defects.

4.1 Collection of data

All input data have been collected with a handheld device (a Nåiden PerCon 3), which record simultaneous vibration measurements in 3 orthogonal directions (hor-



Figure 9: A block diagram of the PerCon3 measurement device.

horizontal, vertical and axial). An accelerometer (with sensitivity 100 mV/g) is magnetically attached to fixed measurement points on the machine. The accelerometer produces a charge that is proportional to the acceleration of the surface. This charge is high-pass filtered to adjust for transducer bias and then measured according to Figure 9. Finally, in all our evaluations, we also highpass filter the measurement a with the cut-off frequency 200 Hz, which is chosen so that we do not need to worry about typical low-frequency disturbers, such as the line frequency or the rotational frequency of the axis.

5 Experimental results

Using MATLAB and all 103 test signals, we have evaluated several different combinations of the basic methods described in Section 3. In the following subsections, we describe and present a more extensive and systematic evaluation of the four best performing methods so far. Then we summarize all experimental results in Section 5.4 and give further conclusions and suggestions for future improvements in Section 6.

The following methods were developed for another set of test signals and are therefore in no way optimized for providing good performance with the test signals at hand. In the classification plots (such as Figure 11 (b)), each test signal corresponds to one plotted point. Functional and defect bearings are denoted with dots and stars respectively. As a simple classification rule we have separated the stars from the dots with a threshold line, which can be used to classify new signals. We have chosen a line that minimizes the *misclassification rate*:

$$\text{Misclassification rate} = \frac{\text{Number of points on wrong side of the line}}{\text{Total number of points}}.$$

Note, however, that the misclassification rate depends on the mixture of test signals. For example, if almost no test signal comes from a machine with a defect bearing, one would get a good misclassification rate for a “method” that classifies all bearings as functional. However, roughly half of our test signals are from machines with a defect bearing, so the misclassification ratio is a useful measure for comparing different methods. Two other performance measures that are important from an implementation point of view are the

$$\text{false alarm rate} = \frac{\text{number of functional bearings detected as “defect”}}{\text{number of functional bearing test signals}}$$

and the

$$\text{miss rate} = \frac{\text{number of defect bearings detected as “functional”}}{\text{number of defect bearing test signals}}.$$

If the mixture of test signals is “realistic” (for a given (type of) industrial environment), then the false alarm rate is an estimate of the probability that the method detects a defect when measuring on a functional bearing. Similarly, the miss rate is an estimate of the probability that the method fails to detect any bearing faults in a measurement from a machine with a bearing fault. There is always a trade-off between these probabilities and it depends on the type of machine and environment which of these probabilities is the most important one to minimize. Thus any method can be fine-tuned for a particular type of machine in the following way: First find the minimum misclassification rate for a (sufficiently large and realistic) set of test signals. Then adjust the classification line so that the misclassification ratio remains (close to) minimal and the proportion between false alarm rate and miss rate is satisfactory for the application at hand.

Note, finally, that some of the methods not presented here also may perform well after further refinements, especially feature extraction, which gave some very promising first results but still is not explored thoroughly enough for any final conclusions.

5.1 The envelope method

For each test signal and measurement direction, we have first applied an 150–10 000 Hz bandpass filter and demodulation as in Figure 8. Then we add the resulting envelopes in l_2 -sense ($e = \sqrt{e_x^2 + e_y^2 + e_z^2}$) before computing the FFT. In Figure 10 (a) we plot the results for two measurements on a condensate pump. Note the clearly visible peaks at multiples of the inner ring impact frequency 120 Hz for the measurement on a defect bearing. These peaks are missing for the other signal, which is an identical measurement after replacing the faulty bearing.

Figures 10 (b) and (c) show the result of applying the following automatic classification to all test signals: Due to measurement precision (usually about 2 %), the impact frequencies in (2.1) are known only up to some maximum error ε . Thus, suppose that we are looking for peaks at multiples of a repetition frequency $f \pm \varepsilon$, known up to a maximum error ε . Then, for $n = 1, 2, 3$, the n th peak (if any) is in the interval $I_n \stackrel{\text{def}}{=} [n(f - \varepsilon), n(f + \varepsilon)]$. Thus, by dividing the maximum amplitude in I_n with the median value between the intervals I_n and I_{n+1} we get a *peak-to-median ratio* that we use as a measure of the size of the biggest peak in I_n . Since our measurement device has a fixed maximum signal length, an increasing sampling frequency gives higher frequency resolution, a more precise hit of peak values and, consequently, a higher peak-to-median ratio. Thus, for identical sampling frequency and a fair comparison, we upsample input signals with lower sampling rate to 25.6 kHz (see, e.g., [24]). A noise reduction also improved the

performance of the resulting algorithm:

1. Upsampling to 25.6 kHz.
2. Wavelet packet noise reduction using a Daubechies 9 wavelet), expanding into 9 levels, using Shannon entropy (see, e.g., [2, 21]) and keeping the M largest coefficients, with M chosen to be 20 times the number of expected outbursts. (By experiments we have found that 20 coefficients is more than enough for representing one outburst.)

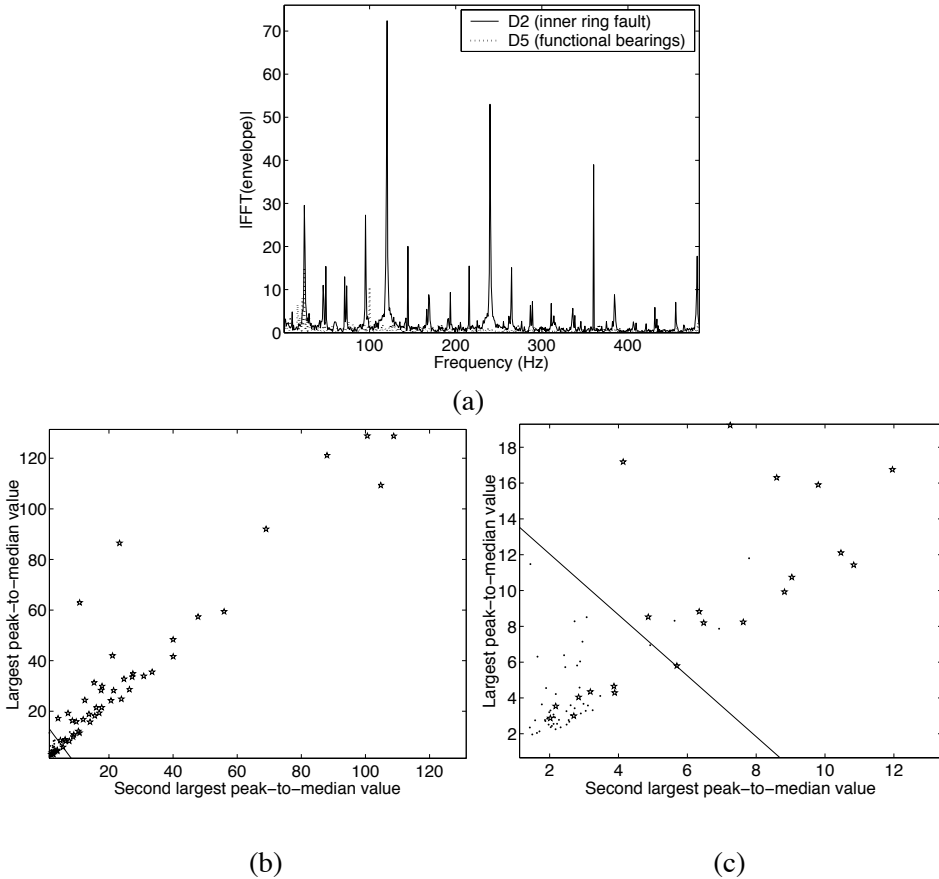


Figure 10: The envelope method: (a) Example plot for measurements on a condensate pump before and after replacing a faulty bearing. (b) Automatic classification (\cdot = functional and \star = defect bearing). The misclassification rate is $10/103 \approx 10\%$. (c) Part of plot (b) in close up.

3. Envelope method computed as described above.
4. Compute peak-to-median ratios for $n = 1, 2, 3$ and for each repetition frequency in (2.1). Keep the two largest and use as coordinates for one point in the plane.

5.2 Periodisation method

In Figure 11 (a), we apply the periodization method (described in Section 3.1) to test rig measurements on bearings that are identical except for an outer ring fault on the one called J1a. In the computations for these plots, the period T in the algorithm corresponds to the outer ring frequency, which gives a very clear “bump” in the plots for J1a, with maximum values 0.54, 0.65 and 0.66. Six smaller maximum values follows when repeating the same periodization computations for J1a with $1/T$ equal to the inner ring and ball repetition frequency, respectively. Thus we choose the two largest maximum values 0.65 and 0.66 to be the coordinates of the corresponding point in Figure 11 (b). Some of our test signals are measured with an older measurement device with less memory, so for a fair comparison, we have evaluated this method only on those 89 (of 103) test signals for which we can set $N = 20$ periods. Thus we end up with the following algorithm:

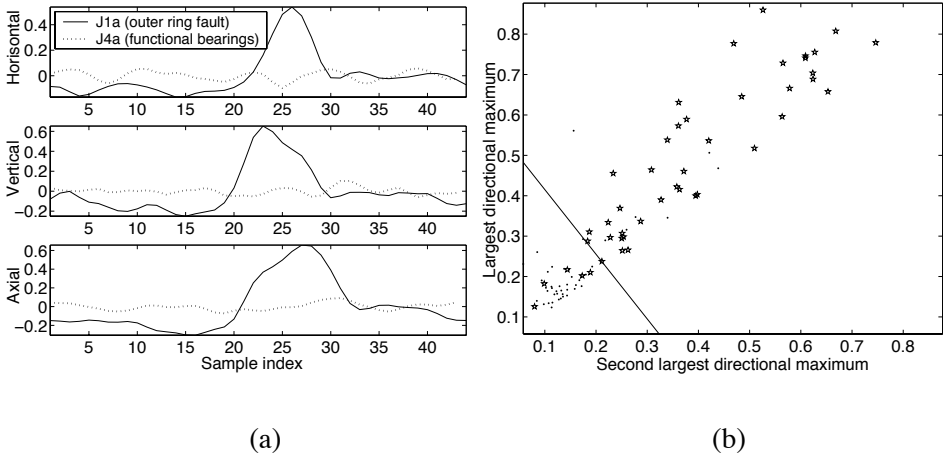


Figure 11: The periodization method applied to test rig measurements on identical bearings with and without outer ring fault: (a) Analysis of signals measurements in horizontal, vertical, and axial direction. (b) Automatic classification (\cdot = functional and \star = defect bearing). The misclassification rate is $12/89 \approx 13\%$.

1. For each repetition frequency in (2.1) and each measurement direction, apply the periodization method and find the maximum value.
2. Use the two largest maxima as coordinates for one point in the plane.

5.3 CWT-based methods

We describe two methods (denoted **CWT1** and **CWT2**) that are based on the continuous wavelet transform $\mathcal{W}_\Psi s(a_k, t)$ of the analyzed signal s , with a *Morlet* wavelet $\Psi(t) = e^{i\omega_0 t - t^2/2}$, $\omega_0 = 5$ and with wavelet center frequencies (see,

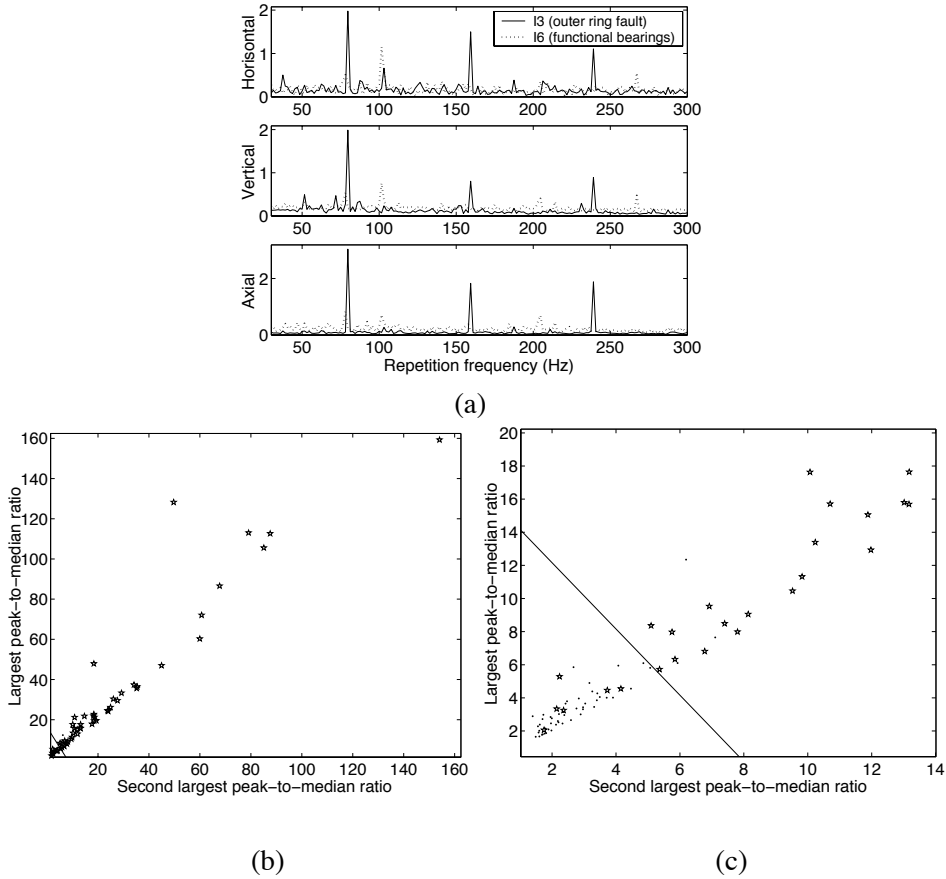


Figure 12: The CWT1 method: (a) Example plot of $\sum_{k=0}^{100} f_k$ for the signals I3 and I6. (b) Automatic classification (\cdot = functional and \star = defect bearing). The misclassification rate is $9/103 \approx 8.7\%$. (c) Part of plot (b) in close up.

e.g., [11])

$$\frac{\omega_0}{a_k} = 20 + k \frac{f_s/2.56 - 20}{100}, \quad k = 0, 1, \dots, 100, \quad (10)$$

where f_s is the sampling frequency of s . Both algorithms analyze the functions

$$e_k \stackrel{\text{def}}{=} |\text{FFT}(|\mathcal{W}_\Psi s(a_k, \cdot)|)|, \quad k = 0, 1, \dots, 100, \quad (11)$$

which is nothing but an application of the envelope method to the restriction of the CWT to frequency ω_0/a_k (the use of a *complex*-valued Morlet wavelet eliminates the need for demodulation).

Hence, if there are some k_1 , k_2 and n such that e_k has maximum amplitude $e_k(n)$ for $k = k_1, k_1+1, \dots, k_2$ and such that $\sum_{k=k_1}^{k_2} e_k(n) / \sum_{k=0}^{100} e_k(n)$ is “close enough” to 1, then one can expect the analyzed signal s to contain some transient and periodically repeating oscillations with oscillation frequency $\approx \omega_0/a_k$ Hz and repetition frequency $\approx n f_s/N$ Hz, where $k_1 \leq k \leq k_2$ and, where N is the length (number of samples) of s . This is the intuitive motivation for how the CWT2-algorithm automatically chooses the oscillation frequencies with largest SNR in measurements on defect bearings, and finds the “most dominating” repetition frequencies at those oscillation frequencies. We begin, however, with the simpler and less adaptive CWT1 algorithm.

CWT1: Figure 12 (a) contains example plots of $\sum_{k=0}^{100} e_k$ for the signals I3 and I6 (from a worm screw pump before and after replacement of a bearing with a large pitting damage with material flaking). For the automatic classification in figures 12 (b) and (c) we have used the following algorithm:

1. For each repetition frequency in (2.1) and each measurement direction,
 - (a) compute $\sum_{k=0}^{100} e_k$ with e_k defined in (11).
 - (b) Apply the same automatic evaluation as for the envelope method in Section 5.1 but keep only the largest peak-to-median ratio.
2. Choose the two largest peak-to-median ratios computed in step (1).

CWT2: In Figure 13 (a) we have applied the basic steps of the method CWT2 to signal H2 (from a drying cylinder bearing with unevenly distributed pits in the outer race): For each e_k in (11), we have plotted the amplitude and the associated repetition frequency $n f_s/N$ of the 3 largest peaks in the topmost two plots. For every point at the y -axis of the second plot, we have then checked at which oscillation frequencies (if any) this is the dominating repetition frequency, summed those peak amplitudes, divided with the sum of all peak values and plotted the result in

subplot 3. Then we repeated the last step for the two other curves in the second plot to get the lowermost two plots. This type of figures gives a rather good overview

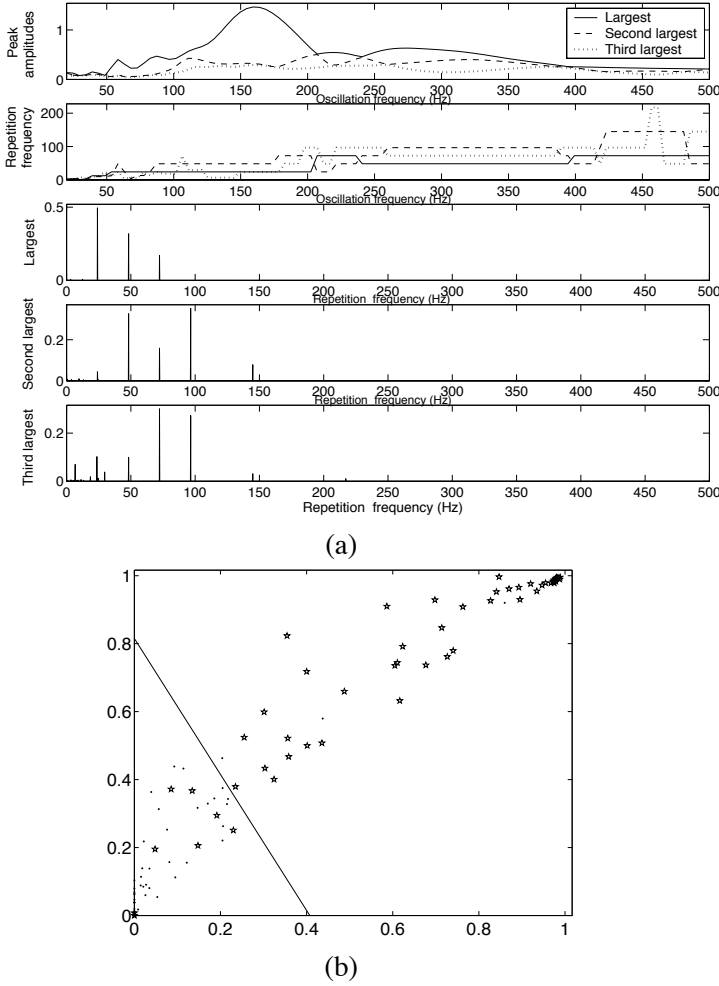


Figure 13: CWT2 method example plot for the signal H2: (a) The topmost two subplots show the amplitude and repetition frequency nf_s/N (plotted as functions of the oscillation frequency ω_0/a_k) of the largest, second largest and third largest peak of each e_k . The remaining subplots show the associated relative peak amplitudes (computed as described in the text) at each repetition frequency. (b) Automatic classification (\cdot = functional and \star = defect bearing). The misclassification rate is $11/103 \approx 10.7\%$.

of the dominating repetition frequencies at different oscillation frequencies. For example, we can clearly see both the outer ring frequency 24 Hz and several of its harmonics.

The full algorithm for finding potentially interesting k s, corresponding repetition frequencies and producing the classification plots in Figure 13 (b), goes as follows:

1. For each measurement direction and for each repetition frequency $1/T$ in (2.1), do the following.
 - (a) Apply a wavelet packet noise reduction with Daubechies 9 wavelet, nine levels expansion and keeping the 10 % largest coefficients (see, e.g., [2, 21]).
 - (b) For $n = 1, 2, \dots, N$ and for $m = 1, 2, 3$, let K_m be the set of integers k such that $e_k(n)$ is the amplitude of the m th largest peak and set $S_{m,n} = \sum_{k \in K_m} e_k(n) / \sum_{k=1}^{100} e_k(n)$.
 - (c) Let M be the set of integers n such that nf_s/N is in some neighborhood (depending on with how good precision T is known) of $1/T$, $2/T$ or $3/T$. For $m = 1, 2, 3$, compute $\sum_{n \in M} S_{m,n}$.
2. From all computations of the sum on the previous line, keep the two largest values.

5.4 Summary of experimental results

Table 2.2 is a summary of the registered misclassifications for our best performing methods. We describe different possible causes for these misclassifications in [9]. The most frequent suggestions are low signal to noise ratio (SNR) and/or an impact frequency that coincides with twice the feeding frequency of the motor.

We have chosen test signals for which all bearing defects are clearly visible and described in more detail in [9, p. 58–64]. For those sharp defects that were detected in plots like Figure 13 (b), the plotted points are generally more far away from the classification line for defects in otherwise smooth inner and outer ring surfaces (as expected in the case of model deviations or lower SNR).

Most methods (with periodization as a notable exception) have some problems with signals F1–4 (see Table 2.2), which are measured on a slowly rotating (93 rpm) drying cylinder with an outer race bearing defect. Here we think that one important reason for the high miss rate is a low SNR caused by the fact that all signals are bandpass filtered with the same bandpass filter and a lower cutoff-frequency 150 Hz, which is very close to and interferes with the oscillation frequency.

We note also that although our methods primarily were designed for well-localized single defects, some unevenly distributed defects, like signal O1–3 (large pitting damage and additional axial cracks along the entire raceway) and H1–4 (unevenly distributed damages), were correctly detected, by all methods. Still, some others (like F1–4, which have visible fatigue damages with pitting on 1/3 of the circumference of the outer race) was not.

So, altogether the above observations indicate a combination of both model dependence and robustness against model errors. Still, the misclassification rates in Table 2.2 show that, at this point, there is more or less an even race between these four methods, so we consider it worthwhile to continue refining all of them, for example according to our suggestions in next section.

Miss	Envelope	Periodization	CWT 1	CWT 2
C1		•		•
F1	•		•	
F2	•		•	•
F3	•		•	
F4	•		•	•
H5			•	
K1b		•		
L2a	•		•	•
N1a	•	•	•	•
N1b	•	•		•
N2a				•
N2b		•		•
False alarm				
A1	•	•	•	•
A2	•	•		
A3		•		
B5		•	•	
B6		•		
D4		•		
E6				•
F7		•		
I6				•
M1	•			
Misclassification rate	$\frac{10}{103} \approx 10\%$	$\frac{12}{89} \approx 13\%$	$\frac{9}{103} \approx 9\%$	$\frac{11}{103} \approx 11\%$

Table 2.2: For the methods with lowest misclassification ratios, all misclassification occurred for the above 22 (of 103) test signals (described in detail in in [9, p. 58–64]).

6 Conclusions and suggested improvements

From a theoretical point of view, we concluded that wavelet-techniques are particularly well suited for bearing monitoring methods that makes use of our signal and noise model but without being too sensitive to inevitable deviations from this model (due to the big variety of different machines and industrial environments).

From our experimental results, we conclude that our four best performing methods (and some more) all are good candidates for further refinements towards really good methods. Right now, they are already fully automatic, there is a lot of thought behind all considered methods, some trial and error with test signals for improvements and then our large systematic test to rule out the four currently best ones. Still, we have chosen to test many (combinations of) methods rather than choosing one or a few and really start optimizing. Hence we want to point out both some recommended improvements and a few more variations and alternatives that could deserve some closer study.

6.1 Suggested improvements

Trend charts recall from Section 3 that our methods only analyze the *shape* of the signal. Hence, the probably most evident route to improved performance is to also use historical data, trending (see, e.g., [34, 35]) or comparison with some other known reference values.

Classification line: We only have one set of test signals both for choosing optimal classification line and for the classification. For more decisive evaluations, it would be better to use two separate and large sets of representative and well-classified test signals. Moreover, although our classification lines in \mathbb{R}^2 are practical for visual demonstrations, for optimal performance, one should probably use some other \mathbb{R}^n and a standard classification method, such as linear discriminant analysis [10]. (For bearing monitoring, or related problems, classification methods based on pattern recognition, artificial neural network and expert system based on fuzzy logic have also been used, see e.g. [1, 5, 18, 19, 26, 29, 30].)

Adapt methods to signal and environment characteristics: Contrary to the classification line, our methods were developed and tested on another (much smaller) set of test functions. Then they were used without changes on our test signals, instead of adapting crucial parts like as deconvolution bandpass filters to usually known signal characteristics, such as in the following concrete examples:

- Improve model correctness by adjusting bandpass filters to block frequencies where model deviations or disturbing vibrations are known to exist (as described in the bullet list in Section 2.4) but not too close to the bearing impact oscillation frequency (as for signals F1–4 in Section 5.4).
- Another example (mentioned in Section 5.4) is some misclassifications of functional bearings for which twice the roller frequency coincided with twice the motor feeding frequency. This is a common vibration frequency in AC motors but defect rollers are very unusual, so by not checking for roller defects, one should get lower false alarm rate without a corresponding increase of the miss rate.

Adapt measurement parameters to method and environment characteristics:

We have used test signals with sampling frequencies ranging from 512 to 25 600 Hz and with signal lengths 4 096–16 384 samples. These parameters were not optimized for any particular method or important system parameters (such as resonance frequency or impact frequency). This is sometimes unavoidable (e.g. depending on available measurement equipment) but whenever possible, we recommend a more careful choice for each environment (or other solutions, such as the upsampling in the envelope method). See (2) below for a concrete example.

Use full wavelet packet tree instead of just the nine levels used in the envelope and CWT2 methods (for time-saving reasons).

Parameter choices etc: Especially for the wavelet based methods there are loads of parameters, settings and small choices for which a whole lot of thought and experimenting may be needed for finding (in some sense) optimal combinations. For instance, it can be thresholds, entropies, choice of wavelet, how to choose scaling parameters a_k in (10), how they should be summed (e.g., weighted sums or $l_p - sum$) or if the fact that we have synchronized measurements in three orthogonal directions can be exploited in better ways.

6.2 Some other potentially interesting methods and variations

Different “periodicity measures”: We have used either periodization or the FFT as core method for finding impact periodicities in all our methods (although in combination with different other tools in different methods). For this step other variants, such as the following examples, could be worth some testing:

- Use the periodization method but compute the maximum-to-minimum ratio instead of maximum in step 1 of the algorithm (but then without subtracting the mean value, as done by the bandpass filter there).
- One more alternative is to study the matrix whose n th row contain the sample values corresponding to the interval $[(n - 1)T, nT)$ for $n = 1, 2, \dots, N$. The quotient between the two largest singular values of this matrix then reflects how “close to periodic” the signal is (see [15]).

The LDB algorithm (see Section 3.5) is so far only evaluated for a small number of test signals, but deserves a more careful test.

A refined signal model may (or may not) make the tested statistical methods more useful (see sections 2.2, 2.4 and 3.4).

Decrease input SNR As described after (9), SNR is, by matched filter theory, minimized if the input $a = s''$ is replaced with a certain linear combination of s , s' and s'' . As described there, we found no clear improvement of SNR in our simple test, but still, a closer study (possibly in combination with a refined signal model or other improvements described above) may very well lead to large enough SNR improvements to be interesting either in general or for some particular type of environments.

Finally, we summarize our experiences from this project in three basic rules of thumb for developing and applying a good condition monitoring method:

1. Collect any available and relevant data about the system at hand. For example, is it possible to estimate the impulse response? Does any other source of vibration coincide with the impact frequencies the method is designed to alarm for?
2. Given the memory size of the measurement device, choose sampling frequency with care. It must be *large enough* for the algorithm to capture the basic resonance frequency, but also *small enough* to give long enough measurements to capture several impacts.
3. As far as possible, try to adapt all parameters associated with the method for optimal performance with the system and measurement properties described in 1 and 2.

References

- [1] D.C. Baillie and J. Mathew. A comparison of autoregressive modeling techniques for fault diagnosis of rolling element bearings. (10):1–17, 1996.
- [2] Jöran Bergh, Fredrik Ekstedt, and Martin Lindberg. *Wavelets*. Studentlitteratur, Lund, Sweden, 1999.
- [3] S. Braun. The signature analysis of sonic bearing vibration. (SU-27):317–328, 1980.
- [4] S. Braun and B. Datner. Analysis of roller/ball bearing vibrations. *Journal of Mechanical Design*, (101):118–125, 1979.
- [5] H.C. Choe, Y. Wan, and A.K. Chan. Neural pattern identification of railroad wheel-bearing faults from audible acoustic signals: Comparison of FFT, CWT, and DWT features. *Proceedings of the SPIE*, (3078):480–496, 1997.
- [6] G. Dalpiaz and A. Rivola. Condition monitoring and diagnostics in automatic machines: Comparison of vibration analysis techniques. (11):53–73, 1997.
- [7] Ingrid Daubechies. *Ten Lectures on Wavelets*. SIAM, Philadelphia, Pennsylvania, 1992.
- [8] D. Dyer and R.M. Stewart. Analysis of rolling element damage by statistical vibration analysis. *Journal of Mechanical Design*, (100):229–235, 1978.
- [9] Stefan Ericsson, Niklas Grip, Elin Johansson, Lars-Erik Persson, Ronny Sjöberg, and Jan-Olov Strömberg. Automatic detection of local bearing defects in rotating machines — Part I. Research report 2002 - 16 (69 pages), Department of Mathematics, Luleå University of Technology, SE-971 87 Luleå, September 2001.
- [10] Keinosuke Fukunaga. *Introduction to statistical pattern recognition*. Academic Press, Boston, second edition, 1990.
- [11] Niklas Grip. *Wavelet and Gabor Frames and Bases: Approximation, Sampling and Applications*. Doctoral thesis 2002:49, Luleå University of Technology, SE-971 87 Luleå, 2002.
- [12] Karlheinz Gröchenig. *Foundations of Time-Frequency Analysis*. Birkhäuser, 2000.
- [13] Tedric A. Harris. *Rolling Bearing Analysis*. John Wiley & Sons, Inc, fourth edition, 2001.

- [14] Elin Johansson. *Faulty Bearing Detection with Wavelet Feature Extraction*. Masters thesis / 2000:268, Luleå University of Technology, SE-971 87 Luleå, October 2000.
- [15] P.P Kanjilal and Sarbani Palit. On multiple pattern extraction using singular value decomposition. 43(6):1536–1540, September 1995.
- [16] M.D. Ladd and G.R. Wilson. Proportional bandwidth properties of fault indicating tones in a ball bearing system. *IEEE Comput. Soc. Press*, pages 45–49, 1994.
- [17] C. James Li and Jun Ma. Bearing localized defect detection through wavelet decomposition of vibration. In *Sensors and Signal Processing for Manufacturing (Proc. of Winter Annual Meeting of the American Society of Mechanical Engineers)*, volume 55 of *ASME Prod Eng Div Publ PED*, pages 187–196, Anaheim, CA, USA, November 1992. ASME, New York, NY, USA.
- [18] T.I. Liu and J.M. Mengel. Intelligent monitoring of ball bearing conditions. (6):419–431, 1992.
- [19] T.I. Liu, J.H. Singonahalli, and N.R. Iyer. Detection of roller bearing defects using expert system and fuzzy logic. (10):595–614, 1996.
- [20] D. Logan and J. Mathew. Using the correlation dimension for vibration fault diagnosis of rolling element bearing-I. Basic concepts. (10):241–250, 1996.
- [21] Stéphane Mallat. *A wavelet tour of signal processing*. Academic Press, London, second edition, 1999.
- [22] P.D. McFadden and J.D. Smith. Model for the vibration produced by a single point defect in a rolling element bearing. (96):69–82, 1984.
- [23] J. L. Meriam and L.G. Kraige. *Dynamics*, volume 2. John Wiley and Sons, 2nd edition, 1987.
- [24] Alan V. Oppenheim and Ronald W. Schaffer. *Discrete-time signal processing*. Prentice Hall, NJ, USA, 1989.
- [25] Athanasios Papoulis and S. Unnikrishna Pillai. *Probability, Random Variables and Stochastic Processes*. McGraw-Hill, fourth edition, 2001.
- [26] B.A. Paya, I.I. Esat, and M.N.M. Badi. Artificial neural network based fault diagnostics of rotating machinery using wavelet transforms as a preprocessor. (11):751–765, 1997.

- [27] R. B. Randall. *Frequency analysis*. Brüel & Kjær, Nærum, Denmark, 3rd edition, September 1987.
- [28] J. Shiroishi, Y. Li, S. Liang, T. Kurfess, and S. Danyluk. Bearing condition diagnosis via vibration and acoustic emission measurements. (11):693–705, 1997.
- [29] W.J. Staszewski and G.R. Tomlinson. Application of the wavelet transform to fault detection in a spur gear. (8):289–307, 1994.
- [30] W.J. Staszewski, K. Worden, and G.R. Tomlinson. Time-frequency analysis in gearbox fault detection using Wigner-Ville distribution and pattern recognition. (11):673–692, 1997.
- [31] J. Taylor. Identification of bearing defects by spectral analysis. *Journal of Mechanical Design*, (102):199–204, 1980.
- [32] W.J. Wang and P.D. McFadden. Application of orthogonal wavelets to early gear damage detection. (9):497–507, 1995.
- [33] Y.F. Wang and P.J. Kootsookos. Modeling of low shaft speed bearing faults for condition monitoring. (12):415–426, 1998.
- [34] Glenn White. *Introduction to Machine Vibration*. DLI Engineering, 1994.
- [35] Victor Wowk. *Machinery Vibration: Measurement and Analysis*. McGraw-Hill, Inc., N. Y., 1991.
- [36] Y. Wu and R. Du. Feature extraction and assessment using wavelet packets for monitoring of machining processes. (10):29–53, 1996.

